

# IMPACT OF THE MICROSTRUCTURE ON THE SWELLING OF ALUMINUM ALLOYS: CHARACTERIZATION AND MODELLING BASES

Victor Garric<sup>1,4</sup>, Kimberly Colas<sup>1</sup>, Patricia. Donnadieu<sup>2</sup>, Marie Loyer-Prost<sup>3</sup>, Frédéric Leprêtre<sup>3</sup>,  
Véronique Cloute-Cazalaa<sup>1</sup>, Bénédicte Kapusta<sup>1</sup>

<sup>1</sup> *Université Paris-Saclay, CEA, DES-Service d'Etudes des Matériaux Irradiés  
F-91191, Gif-sur-Yvette*

<sup>2</sup> *Université Grenoble Alpes, CNRS, Grenoble INP, SIMaP  
F-38000 Grenoble*

<sup>3</sup> *Université Paris-Saclay, CEA, DES-SRMP-JANNuS  
F-91191, Gif-sur-Yvette, France*

<sup>4</sup> *Now at: Institute for Radiological Protection and Nuclear Safety (IRSN), PSN-EXP/SES/BECEM,  
BP 17, 92262 Fontenay-aux-Roses Cedex, France*

**Keywords:** irradiation, aluminum, modelling, microstructure

## Abstract

Swelling of metals under irradiation is largely studied in the nuclear industry for its impact on the safe and efficient operation of reactors. However, the case of aluminum alloys remains poorly documented as they are exclusively used in nuclear research reactors which operate at lower temperatures than nuclear power plants. Void swelling in aluminum alloys, which results from the cavities induced by the fast neutron flux in reactor, is measurable only at high fluences, for which few measurement points are available. In this study, samples with various quenching rates were used in order to simulate the variations obtainable during the fabrication of large reactor components. A first series of samples were irradiated with heavy ions in single beam ( $\text{Au}^{4+}$ ) to understand the impact of the quenched microstructure on the voids swelling. A second series of samples were irradiated in a triple beam ( $\text{W}^{9+}$ ,  $\text{He}^+$  and  $\text{Si}^+$ ) to simulate the aluminum transmutation occurring inside reactors. Samples were investigated at very fine scale and characterized to understand the key mechanisms of swelling. Then, quantitative measurements of the swelling were performed in each sample. A high dispersion of the swelling values and a higher value are observed after ion irradiation compared to neutron irradiation for a similar irradiation dose, which seems to be related to the very high damage rate created by ion-irradiation. Therefore, it appears relevant to complement the description of swelling in aluminum alloys with a modeling approach. Swelling values from the literature were incorporated into a Brailsford & Bullough swelling model for two different damage rates, after estimating the parameters of the model from the literature. This work

aims at a better comprehension of the swelling of aluminum alloys both from a quantitative and qualitative point of view and draws the basics requirements for future swelling models.

## 1. Introduction

Swelling of metals under irradiation has been widely studied [1–8] since it is one of the most impactful and observable type of damage inside nuclear reactors core. Among the most used metals in core reactors, graphite, beryllium, steels and zirconium alloys have been widely studied. However, in nuclear research reactors (NRR) which operate at lower temperatures than nuclear power plants and are most often not pressurized ( $T_{\text{coolant}} < 60^{\circ}\text{C}$ ,  $P < 20$  bars), aluminum alloys are widely used because of their low neutron absorption, and their reduced cost compared to zirconium alloys. Aluminum alloys, because of their low mechanical properties at high temperatures cannot be used in power reactors [9], but they exhibit good properties around  $100^{\circ}\text{C}$  which makes them materials of choice for NRRs.

Aluminum alloys from the 6000 series (alloys with magnesium and silicon) have been chosen for their high strength due to precipitation hardening. In these alloys, precipitates formed during the artificial ageing improve the mechanical behavior but also lower the swelling under irradiation [10]. This effect is believed to be directly linked with the metastable precipitates playing the role of undefined bias sinks, slowing down the void nucleation and growth.

While displaying a relatively good stability of their mechanical properties under neutron flux, the void swelling behavior of 6000 aluminum alloys under irradiation still remain poorly understood. Knowledge on irradiation effect on 6000 alloy microstructures is mainly coming from experiment conducted on thin plates (less than 5 mm thick) for the automotive industry. For NRR, thick plates (roughly 60 mm side parallelepipeds) with specific thermal treatments are used as widely reported in the literature [11–14]. Microstructure and local properties of 6000 series, depend strongly on the quenching rate of the thermal treatment [15–18]. The low cooling rate of thicker pieces destined for NRRs application has been shown to produce microstructures differing from the one observed in thin plates [19]. Therefore, irradiation studies dedicated to thick plates have to be performed

Regarding irradiation mechanism, swelling of aluminum alloys is complex since it swells both from the formation of voids and from the transmutation of aluminum itself into silicon [20]. Each swelling contribution is induced by a different part of the neutron energy spectrum. Thermal neutrons ( $E < 0.625$  eV) induce transmutation while fast neutrons ( $E > 0.1$  MeV) create vacancies. Consequently, the global swelling is dependent on the thermal to fast neutron ratio. By irradiating different alloys and even irradiating the same alloy after different thermal treatments, Farrell et al. evidenced a high impact of the microstructure on the void swelling of aluminum [21,22]. However, this impact is poorly described and quantified in the literature.

Using ion irradiations with different fluxes on many different microstructures from a 6061-T6 alloy presenting various quenching rates representative of what is obtainable in thick plates, we propose to explore the effect of irradiations on the microstructure then identify the preferential sites for void formation. Then, irradiated samples will be used to quantify the swelling. In the second part of this work, taking into account data from the literature and using some conclusions of our study, a swelling model is implemented [23,24] in order to build the basis of a predictive model for the global swelling at the end of life of aluminum alloys components.

*Results presented in this paper are, for the vast majority, results of a PhD thesis written in 2019 [25].*

## 2. Materials and Method

### 2.1 Material

The source material is a 64x68x160 cm<sup>3</sup> forged and machined block of 6061-T6 aluminum alloy with the composition specified in Table 1. Three 10 cm side cubes have been extracted from this block.

**Table 1 : Composition of the studied alloy with reference to the standard NF EN 573 (%wt)**

	NF EN 573	Casting
Si	0.40-0.8	0.53
Fe	≤ 0.7	0.38
Cu	0.15-0.40	0.22
Mn	≤ 0.15	0.06
Mg	0.8-1.2	1.08
Cr	0.04-0.35	0.18
Ni	≤ 0.05	0.0045
Zn	≤ 0.25	0.22
Ti	≤ 0.15	0.02
Total non specified	≤ 0.15	
Al	Balance	

Three 10 cm side cubes instrumented with thermocouples have been annealed at 530°C during 12h, then quenched in a different fluid (water, oil and air) and finally artificially aged at 175°C during 12h. After the thermal treatment, a numerical simulation has been performed in order to evaluate the cooling rate at every point of the cube. Simulation evidenced four main quenching rate domains: more than 35°C.s<sup>-1</sup> for water temper near surface, 20°C.s<sup>-1</sup> to 30°C.s<sup>-1</sup> for water temper in the center of the cube, about 10°C.s<sup>-1</sup> for oil temper and less than 0.1°C.s<sup>-1</sup> for air temper. Then, samples of the four domains have been extracted from the cubes [19].

## 2.2 Sample preparation

Specimens for irradiation experiments were obtained from foils cut in the heat treated cubes and mechanically polished to 100 µm using 1200 and 2400 SiC grid paper and further punched to obtain 3 mm discs. Then, discs were mirror polished on one side using successively a 3 µm, 1 µm and 0,25 µm diamond paste. As a result the irradiated side is easily differentiated from the backside. After irradiation, chemical mechanical polishing has been used on samples from **T** and **S** groups to obtain a homogeneous removal of the material in order to target the desired depth and therefore the desired damage. The polishing solution was Escil POM 10 at a pH of 9 to 10. In order to control the removed depth during the polishing process, microhardness indentation was performed on each sample before polishing. Every 10 minutes, the indentation mark was measured to estimate the loss of thickness.

For TEM observation, electropolishing was performed on the backside only using a 70% methanol-30% nitric acid solution at -20 °C with a tension of 17 V on a Struers Tenupol-3. The disc frontside was protected from polishing using an Agar Scientific Lacomit varnish. Some TEM cross section samples were prepared by FIB using a FEI Helios Nanolab which was also used for the preparation of Atom Probe Tomography (*APT*) samples.

TEM observation was performed using a FEI TECNAI-G2- 300 kV LaB<sub>6</sub> for imaging and a JEOL-2100F - 200 kV FEG for EDS experiments. APT experiments were performed using a CAMECA® Leap 4000 HR equipment.

## 2.3 Irradiation experiments

Samples from each of the four metallurgical states have been irradiated using different conditions as given in Table 2. For each metallurgical state, 19 bulk TEM samples have been irradiated. All irradiations were performed under temperature regulation to maintain a temperature of 20°C on the backside of the sample holder. All irradiations were performed at the JANNuS-Saclay facility [26].

In this manuscript, ion irradiations and neutron irradiations data from the literature will be compared. Consequently, only dpa values will be taken account in this paper. Vacancies concentrations taken from SRIM [27,28] have been converted into dpa using the following formula :

$$dpa = V \cdot \frac{\Phi}{d}$$

With V the vacancies rate in vacancies.cm<sup>-1</sup>, Φ the ion flux ion in ion.cm<sup>-2</sup> and d the atomic density in atom.cm<sup>-3</sup>.

**Table 2 : Summary of irradiations performed at JANNuS-Saclay [26]. For each condition, 19 samples were irradiated. Dpa was calculated using SRIM in full damage cascade mode [27,28]. The labels given in column 1 will be used further to refer to the corresponding irradiation condition.**



Group	Beam	Ion	Flux (ion/cm <sup>2</sup> .s)	Energy (MeV)	Time (h)	Fluence (ion/cm <sup>2</sup> )	Targeted dpa (observed area)
<b>S</b>	Single	Au <sup>4+</sup>	2.10 <sup>11</sup>	3.5	52h	3.69.10 <sup>16</sup>	100-150
	Single	Au <sup>4+</sup>	2.10 <sup>11</sup>	3.5	36h	1.96.10 <sup>16</sup>	60-90
<b>T</b>	Triple	He <sup>+</sup>	6.17.10 <sup>11</sup>	0.5	5h30	9.95.10 <sup>15</sup>	20
		Si <sup>+</sup>	6.17.10 <sup>11</sup>	2.5	5h30	9.95.10 <sup>15</sup>	
		W <sup>9+</sup>	2.2.10 <sup>11</sup>	13	5h30	3.62.10 <sup>15</sup>	
	Triple	He <sup>+</sup>	6.17.10 <sup>11</sup>	0.5	5h30	9.95.10 <sup>15</sup>	10
		Si <sup>+</sup>	6.17.10 <sup>11</sup>	2.5	5h30	9.95.10 <sup>15</sup>	
		W <sup>9+</sup>	1.1.10 <sup>11</sup>	13	5h30	1.82.10 <sup>15</sup>	
<b>T'</b>	Single	W <sup>9+</sup>	2.2.10 <sup>11</sup>	13	5h30	3.62.10 <sup>15</sup>	<20
<b>M</b>	Single	W <sup>9+</sup>	2.2.10 <sup>11</sup>	20	5h30	4.4.10 <sup>15</sup> ( <i>max</i> )	Multi: 9 to 29
		W <sup>9+</sup>	1.2.10 <sup>11</sup>	20	5h30	2.3.10 <sup>15</sup> ( <i>max</i> )	Multi: 3 to 15
		W <sup>9+</sup>	0.6.10 <sup>11</sup>	20	5h30	1.2.10 <sup>15</sup> ( <i>max</i> )	Multi: 1 to 6

All damage values in dpa in Table 2 are given for the targeted or observed area. Those values are thus not the maximum dpa nor the mean dpa inside the sample. Every dpa profile was calculated using the data from SRIM [27] in a full damage calculation mode. To obtain various and detailed data and perform automated simulation in a wide range of energies, a modified version [28] of pySRIM, originally developed by Ostrouchov [29] has been used. The irradiation profiles obtained for groups **S** (for single irradiation with Au ions), **T** (for triple beam irradiation), and **M** (for single beam irradiation with W) according to SRIM simulations and corrected with the real fluence measured at the end of each experiment are given in the appendix C of the supplementary material.

Irradiations from the **S** group are single beam irradiations using Au<sup>4+</sup> ions at 3.5 MeV. The use of such heavy ions coupled with the irradiation time creates more than 100 dpa on surface of the sample while the peak of damage obtained is around 400 dpa. With two different irradiation times, 52h and 36h, damages on surface are respectively 100-150 dpa and 60-90 dpa. After irradiation, samples are named **S-100** and **S-60**, respectively referring to the lowest dpa estimation.

Irradiations from the **T** group are triple beam irradiations. They use W<sup>9+</sup> ions at high energy (13 MeV), targeting medium damages while beams of helium and silicon are implanting ions in the same area. This type of irradiation reproduces more closely in-core conditions than with single beam irradiation. However, the final fluence values presented here for the helium are equivalent to centuries of irradiation inside reactors. Therefore, results of the **T** group will only be qualitative, and no quantification of the swelling will be given for this condition. **T'** conditions are single beam irradiation using the same flux and fluences than the W<sup>9+</sup> beam from the **T** group. This experiment has been designed to decorrelate the effects of helium and silicon from the damage of tungsten. **T** group irradiations will be referred as **T-Φ** for the highest flux experiment and **T-Φ/2** for the lowest.

Irradiations from the **M** group are low dpa irradiations (<29 dpa) with a high energy beam (20 MeV). During these irradiations, some samples were masked using a thick iron plate while, during the

irradiation, the plate was removed, allowing to have multiple fluence values for a unique flux during a single experiment. Irradiations from this group are used for void swelling quantification and APT experiments only.

### 3. Results

#### 3.1 Prior irradiation characterization

The microstructure of the samples in the four metallurgical states prior to irradiation has been characterized in details as previously reported in [19]. Two types of precipitations were observed at the nanometric and submicronic scale. Another type of particles is observable at the micronic scale. Nevertheless, its relatively large size does not allow any observation with TEM and therefore is only observed with SEM or optical microscopy. The main type of particles present in the matrix (nanometric or submicronic) strongly depends on cooling rate. The nanometric precipitation is known to induce hardening due to its small size, high density and semi-coherency with the aluminum matrix. The composition of these particles is often referred as Al-Mg-Si-Cu precipitates. The submicronic particles, also named dispersoids, are formed during casting and are mostly incoherent with the aluminum matrix. These dispersoids are mainly the Al-Fe-Mn-Si-Cr  $\alpha$  phase.

##### *Nanoprecipitation*

Nanoprecipitates precipitate homogeneously in the matrix. They are elongated needles with a length ranging from 3 to 7 nm with a width not exceeding 3 nm. Some are also spherically-shaped with a mean diameter of 3 nm. In water tempered specimens, the precipitate volume fraction is 3.5 % for the fastest cooling rates ( $> 40^{\circ}\text{C.s}^{-1}$ ) and 2.5 % for the lowest ( $\sim 28^{\circ}\text{C.s}^{-1}$ ). In oil tempered specimens, the volume fraction dropped to 1.7 % for an associated cooling rate of  $10^{\circ}\text{C.s}^{-1}$ . Finally, in air tempered specimens, no nanoprecipitates were observed. This result is consistent with the low cooling rate ( $< 0.1^{\circ}\text{C.s}^{-1}$ ) which does not permit nanoprecipitation. APT experiments have been performed on water temper specimens. Precipitation of AlMgSiCu clusters is observed which is consistent with the precipitates observed in TEM.

##### *Dispersoids*

Dispersoids displayed vary significantly in terms of size and chemical heterogeneity. In water tempered specimens, dispersoids are mostly squared shapes with an equivalent radius between 30 and 300 nm, and are identified as  $\alpha\text{-Al}_8(\text{Fe,Mn,Cr})_2\text{Si}$  plates. EDS analysis often revealed a chemical segregation with iron in the core and chromium in the shell. Some magnesium rich precipitates seem to be growing on these  $\alpha$ -plates. Smaller spherical dispersoids are also identified as coarse  $\text{Mg}_2\text{Si}$  particles not dissolved during annealing. In oil tempered samples, the submicronic particles are more abundant and often presented a chemical heterogeneity characterized by heterogeneous precipitation on these coarse dispersoids. This effect was even more emphasized in air tempered samples where in addition to the dispersoids and square  $\alpha$ -plates, a dense population of needle-shaped particles with lengths above  $1\mu\text{m}$

was observed. These long particles seem to have nucleated on the dispersoids. Chemical analysis using EDS showed those particles to be oxide phases containing aluminum and magnesium.

### 3.2 Characterization after irradiation

#### 3.2.1 Water temper

Microstructure examinations of water temper in S-60 and S-100 irradiation conditions (single beam) are given in this section.

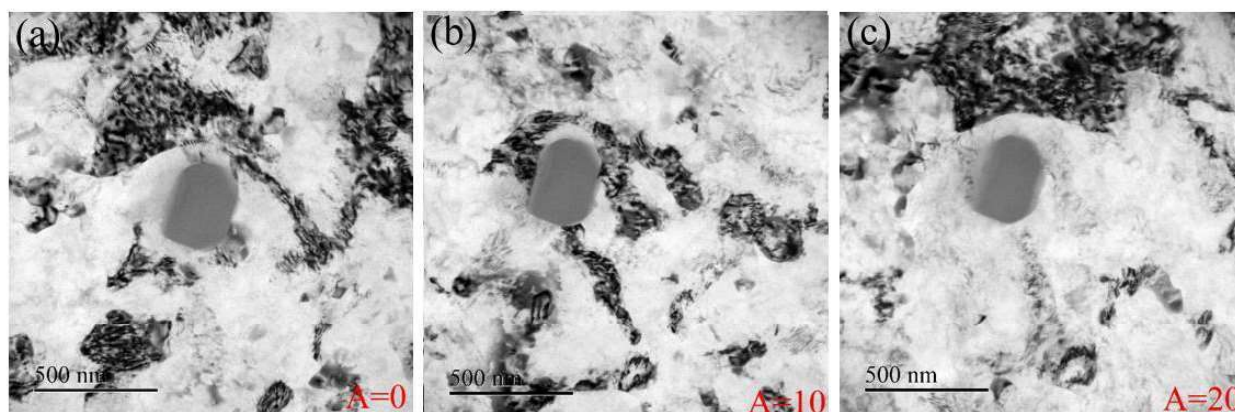


**Figure 1 : Observed microstructure in a S-100 irradiated water temper sample. Tilting around a submicronic precipitate: (a):  $\alpha=0^\circ$ , (b):  $\alpha=10^\circ$ , (c):  $\alpha=20^\circ$**

Figure 1 shows a typical microstructure of a water temper sample at different tilt angles in the same area in S-100 conditions. On Figure 1.a, a grey contrast submicronic particle is observed. The particle is surrounded by diffraction contrast suggesting lots of residual stress in the grain. On Figure 1.b and c, the same area is observed but with an angle of  $10^\circ$  and  $20^\circ$ . The dispersoid pictured the same homogenous contrast. This behavior is typical of an amorphous phase. The localization, size and morphology of these particles are similar than those of the dispersoids observed before irradiation. The dispersoids being crystalline before irradiation, the present observation indicates that amorphization occurs under the beam. This observation was reproduced in all samples in S-100 and S-60 conditions. Concerning small grains with strong diffraction contrast, they are resulting from the sample preparation: to preserve the irradiated area, one side of the disc sample has not been electro-polished. They are then considered as an artefact of the sample preparation.

Figure 2 pictures the microstructure of a water temper sample irradiation in S-60 conditions.

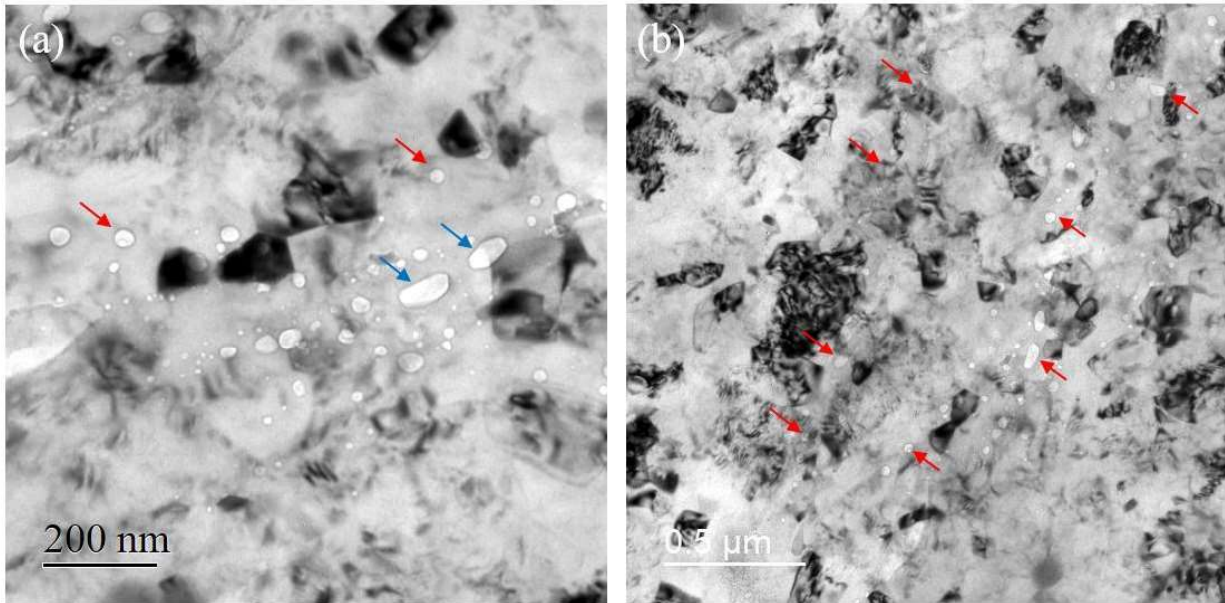
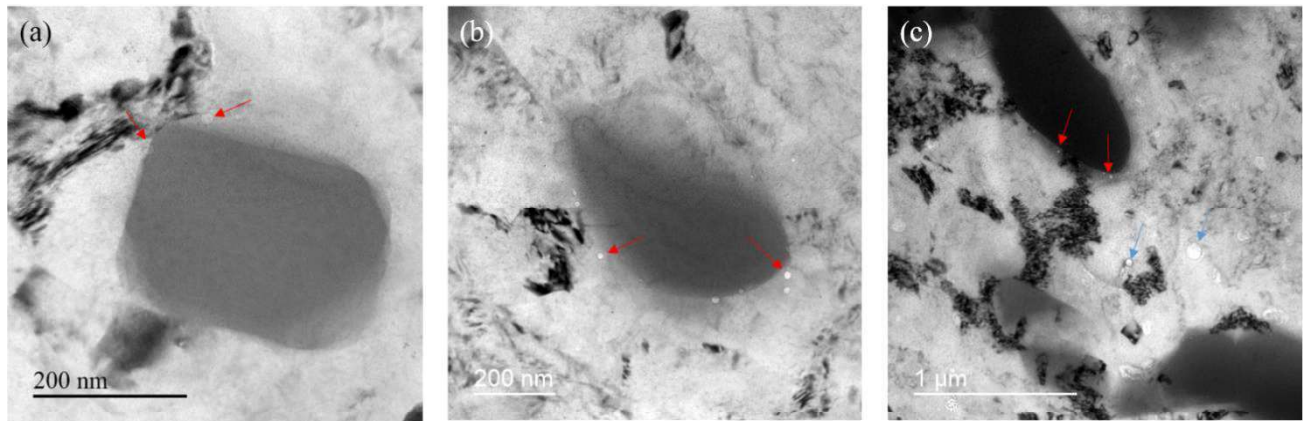


**Figure 2 : Observation of voids inside the aluminum matrix in a water temper sample in S-60 irradiation conditions. (a): at medium magnification, (b): at low magnification**

On Figure 2.a, voids of different shapes are observed. Small and round cavities (red arrow) are observed as well as bigger and elongated ones (blue arrows). Their mean radii range from 5 nm to 70 nm. According to a statistical evaluation performed on multiple pictures, the mean radius is estimated to be about 10 nm for S-100 conditions and 15 nm for S-60 conditions. The mean circularity for both conditions was 0.97 with a standard deviation of 0.06 which shows that most of the voids are round. Volume density of voids pictured a mean number of  $1.09.10^{20}$  voids. $m^{-3}$  for S-60 conditions and a mean number of  $5.31.10^{20}$  voids. $m^{-3}$  for S-100 conditions assuming a 100 nm thickness (further density measurements presented in this article will assume the same hypothesis). Those results are consistent with an increase of voids density with damage.

Figure 2.b pictures the same area at lower magnification. The elongated voids are aligned (red arrows). This observation was repeated in all water tempered specimens, both with S-60 and S-100 conditions. It is consistent with a heterogeneous formation of voids around defects or interfaces (dislocations, grain boundaries for example)

Figure 3 shows several amorphous dispersoids and micronic particles inside the matrix with different irradiation conditions (S-100 and S-60, respectively in Figure 3.a and b). In both cases, a population of round voids (pointed with red arrows) is observed at the interface between the matrix and the particle. Figure 3.c shows a microscopic particle in S-100 conditions. Due to the particle dimensions, it is not possible to test whether the particle is crystalline or amorphous. However, voids nucleate at the particle-matrix interface (red arrows) similarly than for dispersoids.



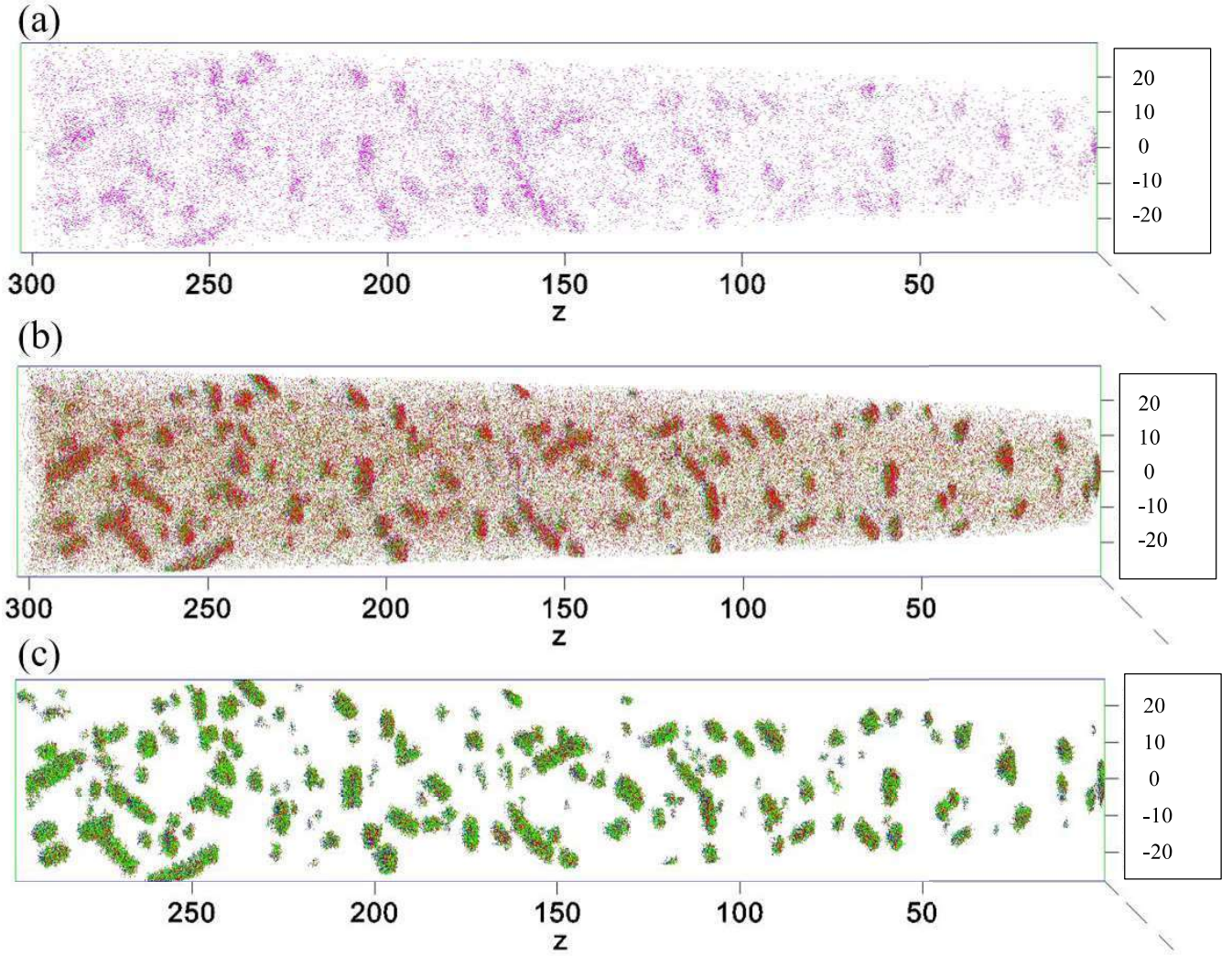
**Figure 3 : Observation near the interface of dispersoids and intermetallic phases in different conditions: (a): S-100, (b): S-60, (c): S-100. Red arrows point at voids at the matrix-phase interface. Blue arrows are pointing voids inside the matrix**

Figure 4 shows APT results in a tip-shaped sample at low dpa conditions (15 dpa from M group irradiation). Due to the highly damaged material, APT could not be performed properly in S-60 and S-100 conditions because the high density of voids makes the tip blow up under high voltage.

Firstly, clusters of magnesium, copper and silicon are observed. They are seen to be needle shaped which is typical of hardening precipitates. This observation is consistent with the nanoprecipitation observed before irradiation. Very small clusters ( $r \sim 1$  nm) are also detected in the analysis. The size of these clusters is equivalent to that of GP zones which are the precursors of  $\beta''$  precipitation sequence.

Clusters of zinc (Figure 4.a) coinciding with Al-Mg-Si-Cu clusters (Figure 4.b) are observed. Before irradiation, zinc is in solid solution and is not measured inside AlMgSiCu clusters. The presence of Zn in the Al-Mg-Si-Cu clusters is consistent with the aggregation of zinc toward nanoprecipitates under irradiation. Going further, a k-mean cluster analysis has been performed. The goal of this analysis is to understand if the presence of Zn with Mg, Si and Cu can be considered as a co-clustering or precipitation. To achieve this analysis, the same parameters as in MgSiCu clusters were taken. Results of the clustering analysis, are presented Figure 4.c. The algorithm reveals clustering in the same areas than in Figure 4.b suggesting these areas are effective Mg, Si, Cu, Zn clusters. This observation shows that zinc migrates from a homogeneous solid solution distribution in unirradiated material to co-clustering with existing precipitates under irradiation.





**Figure 4 : APT experiments in single beam water after M-15 irradiation conditions. Display of (a): Zn atoms, (b) Zn, Mg, Si and Cu atoms, (c): result of Zn, Mg, Si, Cu clustering. All units are in nm**

### 3.2.2 Oil temper

Microstructure examinations of oil tempered specimens in single beam irradiation are given in this section. It is important to remind that, due to technical issues, oil temper specimens were not irradiated in the S-100 experiment.

Figure 5 pictures the microstructure of oil temper in S-60 conditions. A population of mostly spherical voids is observed. Their mean size is ranging from 5 nm to 65 nm. The associated volume density is  $3.02 \cdot 10^{20} \text{ voids.m}^{-3}$ . They are inside the matrix and aligned as illustrated by the high magnification view (Figure 5.b). These alignments are similar to those observed in water temper samples as described in the previous section.

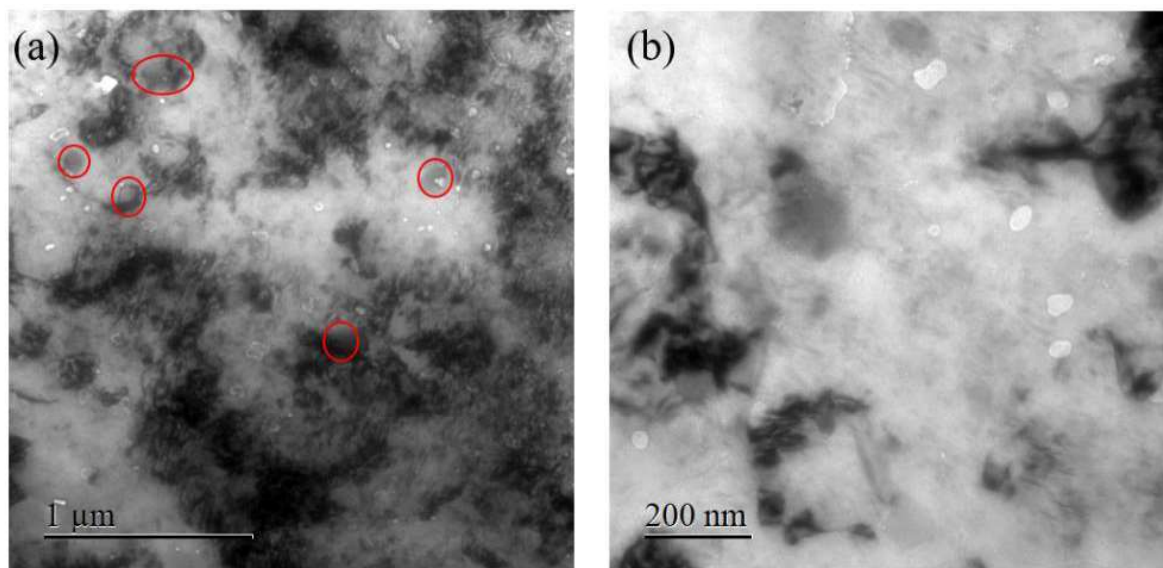


**Figure 5 : Voids seen in oil temper after S-60 irradiation conditions: (a): unaligned and undefined voids around dispersoids, (b): aligned cavities.**

EDS experiments (see supplementary material) on dispersoids after irradiation pictured segregation of elements similar to the one observed prior irradiation. However, the morphology of some particles suggests partial dissolution has occurred during irradiation.

### 3.2.3 Air temper

Figure 6 shows TEM micrographs of the air temper microstructure after S-100 irradiation conditions recorded at different magnifications. A population of nanoscaled voids appears homogenously distributed in the whole matrix. Unlike the observations in water and oil temper, voids are present in the whole matrix and do not exceed 5 nm in diameter.

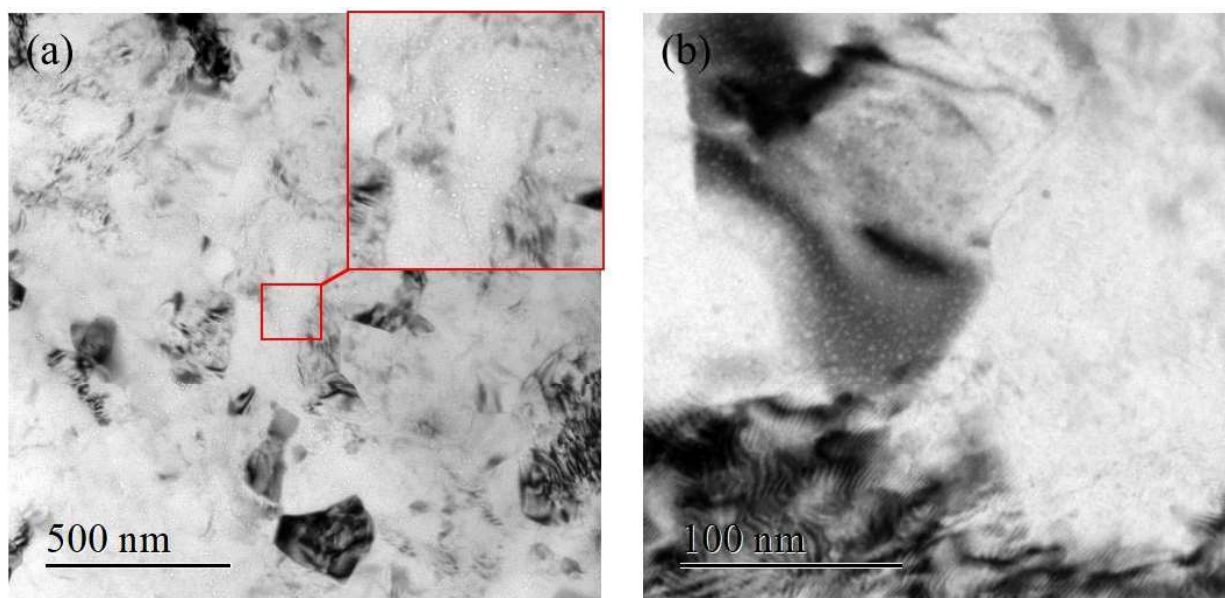


**Figure 6 : General aspect of the air temper microstructure after S-100 irradiation conditions. (a): large view, (b): closer view**



Some specimen from S-100 conditions were specifically polished to perform observation in an area where the irradiation dose is 10 dpa. Dispersoids observed in Figure 7.a. are not affected by irradiation (green circled areas). However, as pointed by the red dotted line in Figure 7.a. a very high density of voids is observed in areas with the same morphology as the elongated coarse oxide particles. This observation suggests that at low damage values, the coarse oxide particles tend to dissolve. Two different behaviors of the submicronic particles under irradiation are observed here: - dispersoids (intermetallic), while being amorphized at higher dose, remain stable for lower irradiation doses; -coarse particles (oxides) are seen to dissolve in the early stages of irradiation.

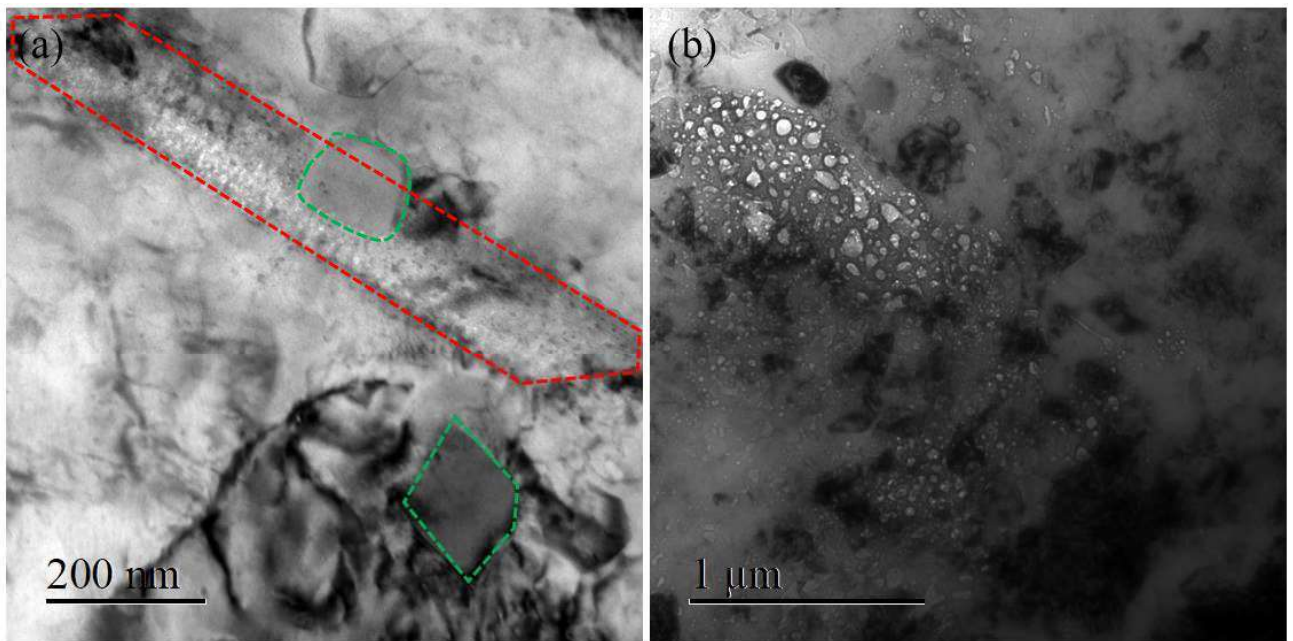


**Figure 7 : (a): observation of a trace of a submicronic particle at low dpa in air quenched specimen irradiated with S-100 conditions. Specimen was polished to observe the area irradiated at 10 dpa. The coarse dispersoid circled in red is dissolving around a phases circled in green, (b): local heavy concentration of large voids observed in an air tempered, S-100 irradiated specimen**

Figure 7.b is picturing a large view of the microstructure in the S-100 irradiation condition for an air temper specimen. Besides the small voids homogeneously distributed in the matrix, some areas are locally displaying many large voids. The size and the roughly globular shape of these areas are similar to the micronic particles observed in the non-irradiated state. This observation was only made for air temper specimens.

As a summary, in air quenched specimen, three types of voids have been identified: aligned voids, nanocavities in the matrix and local heavy concentrations of irregular voids.

Table 3 summarizes the mean density measured for specimens in S-100 and S-60 conditions. It is observed that each type of voids pictures a different order of magnitude in terms of voids density.



**Table 3 : density of voids in air temper depending of the irradiation conditions and the type of voids**

	<b>S-100</b>			<b>S-60</b>		
	Aligned	Nano	Irregular	Aligned	Nano	Irregular
<b>N<sub>0</sub></b> <b>(voids.m<sup>-3</sup>)</b>	1.20	190	19.3	1.65	186	15.6

Figure 8 is a schematized diagram explaining the formation of voids during single beam irradiations in 6000 aluminum alloys as observed in this study. Three main microstructures are pictured before and after irradiation. They are described not by the quench fluid but by their quench rate, which is compared with  $v_{crit}$ , the critical cooling rate according to the literature.  $v_{crit}$  is known to be equal to  $10^{\circ}\text{C.s}^{-1}$  [30,31].

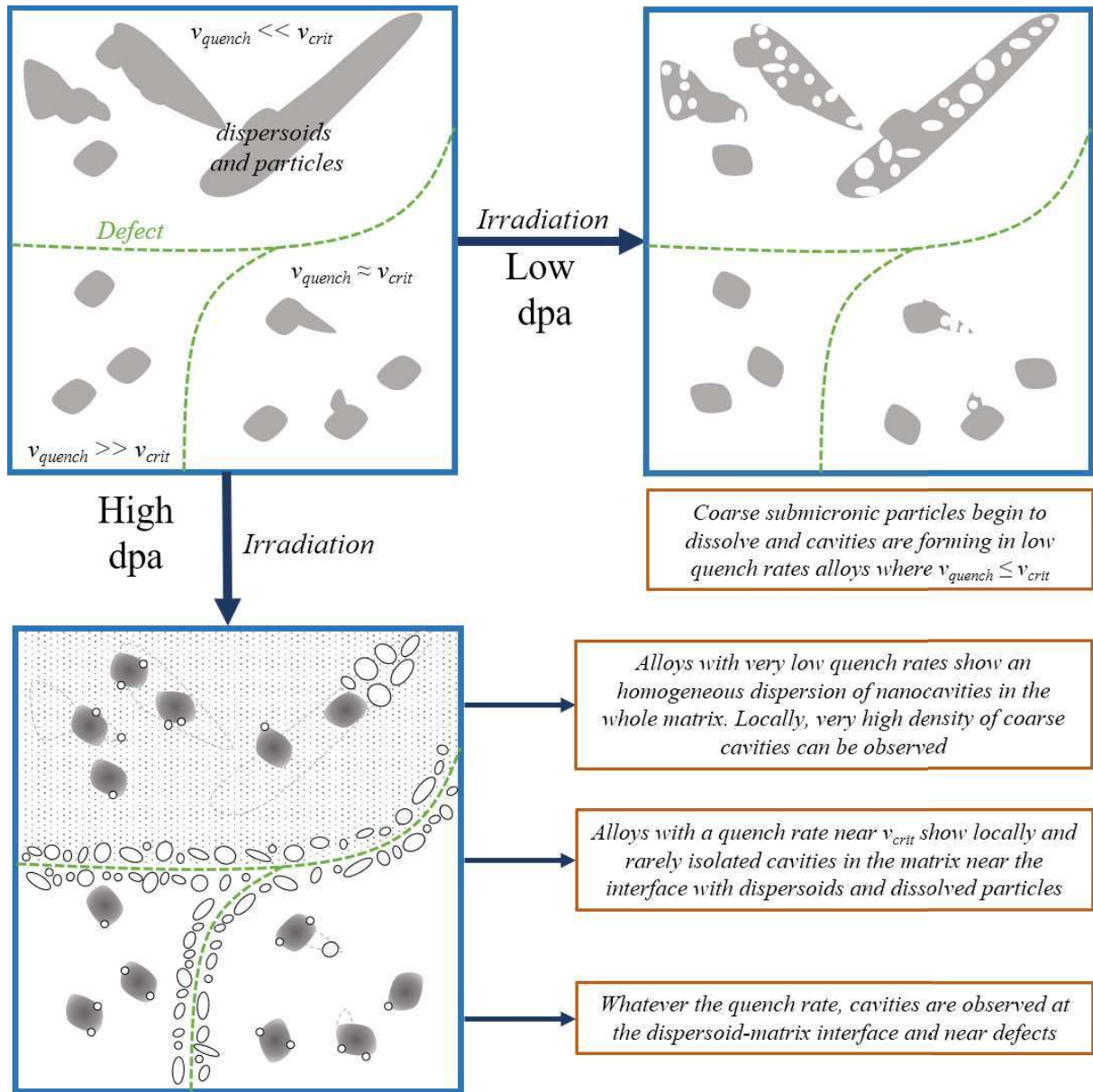


**Figure 8 :** A schematic diagram on the formation of voids in aluminum alloys depending on the initial microstructure.  $v_{crit}$  is the critical quenching rate according to the literature ( $10^{\circ}\text{C.s}^{-1}$ )

### 3.3 Triple beam irradiation experiments

Experiments under T- $\Phi$  irradiation conditions were performed in order to simulate, compare and understand the impact of helium and silicon created by the transmutation of aluminum. However, if the silicon dose was close to what is observable after ten years inside a research reactor, the helium dose implanted is close to thousands of years which is not comparable to anything realistic. Therefore, results presented in this section will only be analyzed in a qualitative way.

#### 3.3.1 Water temper

Figure 9.a presents a TEM picture in water temper after T- $\Phi$  irradiation conditions, revealing a homogeneous dispersion of nanoscale cavities (size  $\sim 2\text{nm}$ ) inside the whole aluminum matrix of the

implanted area. To determine whether these cavities were voids or gaz bubbles, an EELS analysis has been carried out in this area. The EELS spectrum (Figure 9.b) displays an intense peak at 22 eV which is characteristic of the presence of helium. This is consistent with the formation of helium bubbles during the triple beam irradiation.

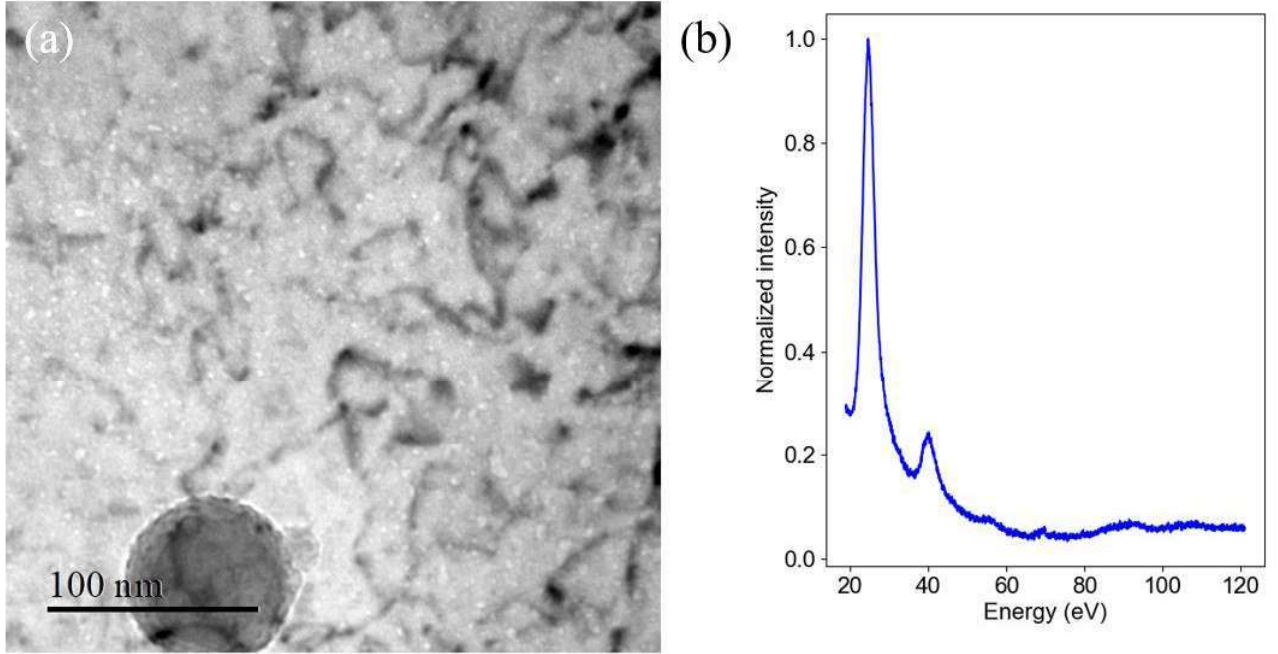


**Figure 9 : (a): area with nanoscale cavities inside watered tempered specimen in  $T-\Phi$  conditions, (b): EELS analysis in an area containing bubbles**

The bubbles had a mean radius of 1.5 nm. The area and circularity of the bubbles was performed after thresholding pictures using the Phansalkar method [32]. Results presented in Table 4 show a mean area of 4.2 nm<sup>2</sup> (associated mean radius 1.15 nm) for  $T-\Phi/2$  conditions and a mean area of 7.0 nm<sup>2</sup> (associated mean radius : 1.5 nm) for  $T-\Phi$  conditions. This observation implies that doubling the fluence globally doubles the mean area of the bubbles. For the  $T-\Phi$  and  $T-\Phi/2$  conditions, a very high standard deviation of the areas (higher than the mean value) was observed. Circularity was low but considering the size of the bubbles and the resolution of the picture, such values are not unexpected.

**Table 4: Statistical analysis of bubbles size and circularity in  $T-\Phi$  and  $T-\Phi/2$  conditions in water temper specimens**

	$\Phi/2$		$\Phi$	
	Mean	Std. Dev.	Mean	Std. Dev
<b>Area (nm<sup>2</sup>)</b>	4.2	3.6	7.0	14.8
<b>Circularity</b>	0.67	0.17	0.55	0.23

Characterization of the nanoprecipitation after  $T-\Phi$  irradiation conditions have been performed. Nanoprecipitation was still observed after  $T-\Phi$  irradiation, but some precipitates observable in bright

field along  $\langle 100 \rangle$  zone axis were no longer observable in dark field in  $\langle 001 \rangle$  zone axis conditions. This suggest the presence of a new family of precipitates. This phenomenon has never been observed in S-100 or S-60 conditions in any temper. However it is consistent with the formation of a new nanoprecipitates family under irradiation as reported by Flament et al. [33].

### 3.3.2 Oil temper

TEM observation in the case of oil temper after T- $\Phi$  irradiation were performed on a FIB cross section sample. This cross section has been cut in an irradiated disc sample in order to observe the sample along the implantation profile. Figure 10.a shows the FIB section in TEM bright field at low magnification with the damage and implantation profiles over the picture. The right side of the picture corresponds to the edge of the surface exposed to ions during irradiations. The rim delimited by red and blue solid lines is the area where nanograins formed both by the preparation technique and irradiation are located. Figure 10.b pictures a high density of bubbles in the peak implantation area: bubbles have a mean radius of 1.5 nm as in water temper in the same T- $\Phi$  condition.

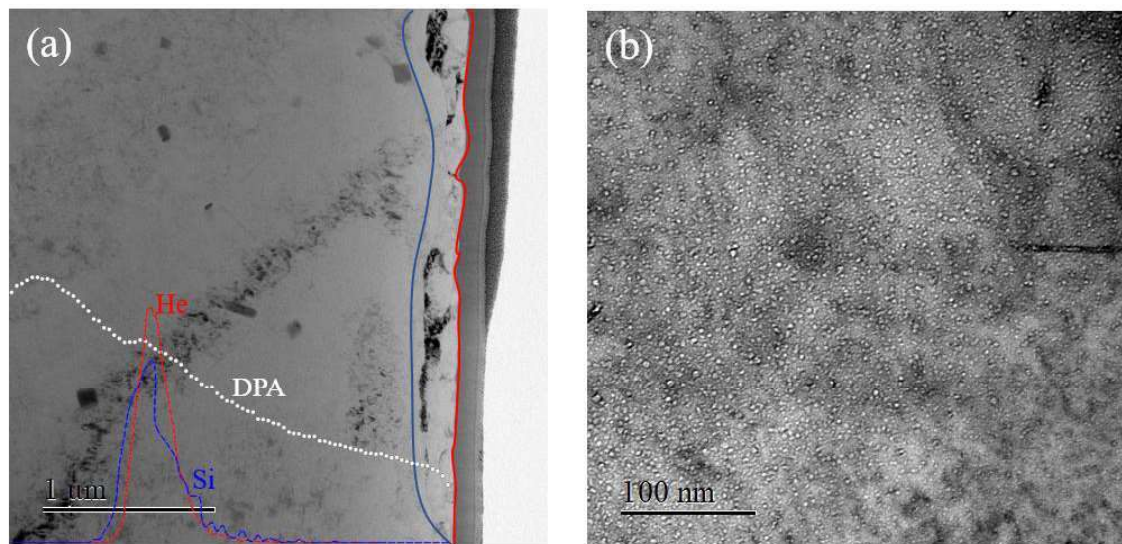


**Figure 10 : Observation in T- $\Phi$  conditions in oil temper inside a FIB sample: (a): damage and implantation profiles in the specimen, (b): bubbles observed in the peak implantation area**

Figure 11 shows a dispersoid in an oil tempered specimen after T- $\Phi/2$  irradiation conditions. In the vicinity of the dispersoid (area delimited by the blue dotted line), the density of bubbles seems to be lower than inside the matrix. Some larger bubbles are observed very close to matrix-dispersoid interface. However, between interface and blue dots lines, the number of bubbles seems to decrease.



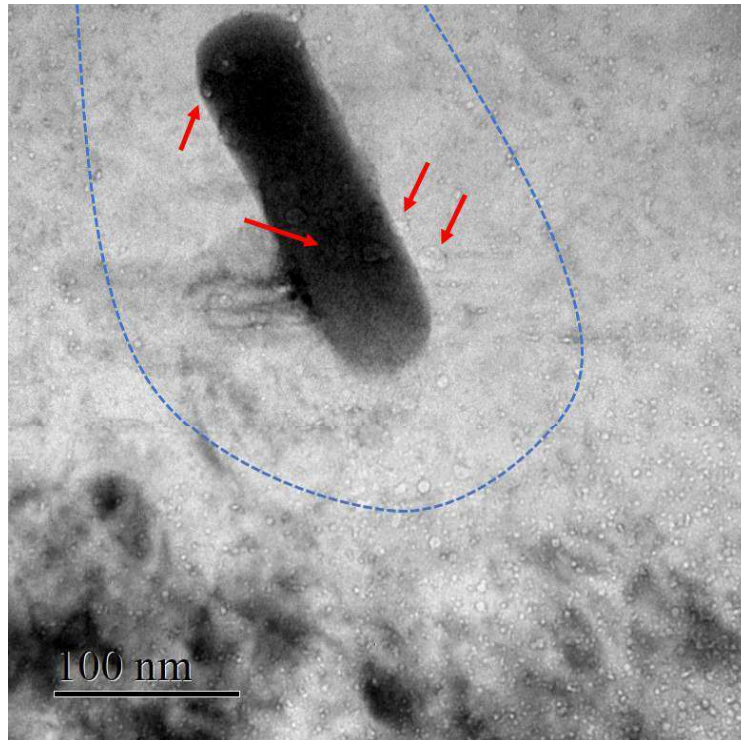


*Figure 11 : Dispersoid observed in oil temper on a T- $\Phi$  FIB sample.*

### 3.3.3 Air temper

Air temper samples irradiated with T- $\Phi$  and T- $\Phi/2$  irradiation conditions displayed an intense population of bubbles as presented Figure 12.

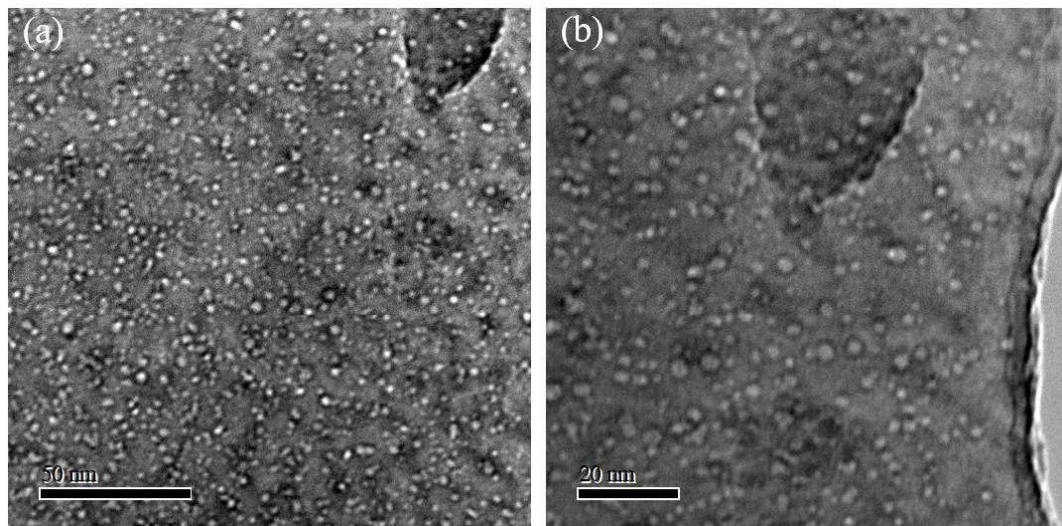


*Figure 12 : Bubbles inside the air temper with T- $\Phi$  irradiation conditions.*

Coarse particles (oxides) observed prior irradiation were not observed after irradiation in both T- $\Phi$  and T- $\Phi/2$  conditions. At low dpa (Figure 13) the presence of a dispersoid displaying a high density of bubbles is observed near traces of coarse particles. This is consistent with the observations made in S-

100/S-60 conditions. These results suggest that a dissolution of coarse particles occurs in the early stages of irradiation.

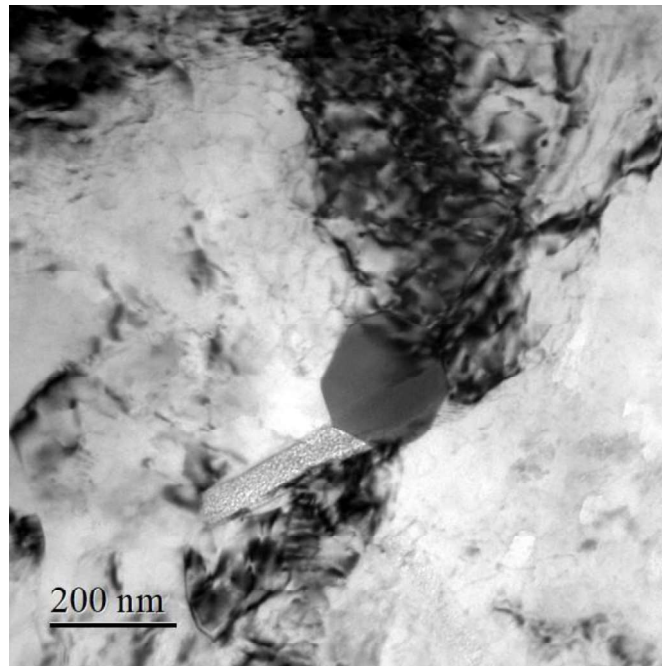


*Figure 13 : Dissolution of a coarse particle near a dispersoid at low DPA in air temper after T- $\Phi$  irradiation conditions.*

Finally, formation of large voids, as observed in S-60 and S-100 conditions, were not observed in both T- $\Phi$  and T- $\Phi/2$  conditions.

Figure 14 represents schematically the same initial state as provided in Figure 8, but adding a representation of the nanometric scale. The influence of the implantation of silicon and helium during irradiation is represented and the microstructure modification is pictured at both scales.

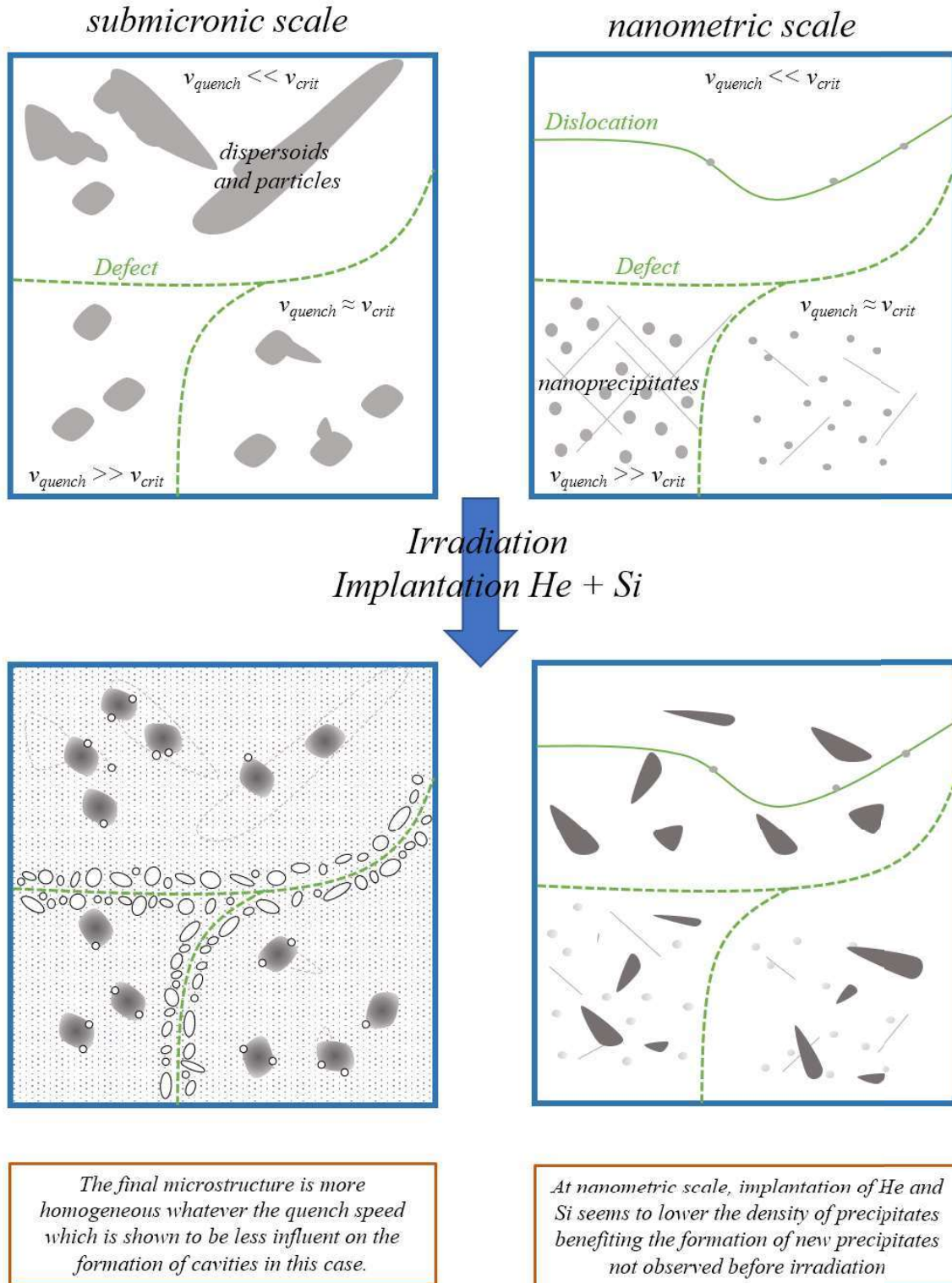


**Figure 14 : Schematic representation of the influence of silicon and helium in the formation of voids under irradiation**

The behavior of 6000 aluminum alloys under irradiation is different for various quench rates and the irradiation conditions. Nanoprecipitation remains stable under irradiation whatever the quench rate, except when silicon and helium are implanted. With T-Φ and T-Φ/2 conditions, another kind of nanoprecipitation appears. Dispersoids amorphized under ion flux whatever the

temper and the irradiation conditions. However, coarse particles (oxides) and heterogeneous precipitates seen in oil and air tempers totally dissolved in the early stages of irradiation. Different nucleation sites have been identified for voids and bubbles. In all tempers, in single beam conditions, voids aligned suggesting a nucleation on dislocations or grain boundaries and also formed at the dispersoid-matrix interfaces. In air temper in single beam conditions, nanometric voids were observed in the whole matrix and local heavy concentration of irregular voids was rarely observed. With triple beam conditions, nanometric voids were observed in the entire matrix for all tempers. The results from this study globally show a strong link between tempering conditions and behavior under irradiation. In addition, specific irradiation conditions (single beam or triple beam with helium and silicon implantation) will also strongly impact the response of the material. In particular helium implantation seems to have a strong impact on the bubble density, and because of the very high helium concentration implanted in our triple beam study, the void swelling has been measured after simple beam irradiations. In order to quantify the total swelling under neutron flux, modeling has been performed as presented in the next paragraph.

#### 4 Modelling

Swelling of aluminum alloys under neutron irradiation has two components: the aluminum transmutation into silicon and void swelling. Estimation of both is critical to estimate a correct swelling of the alloy. Aluminum to silicon transmutation is induced by thermal neutrons ( $E < 0.625$  eV) and void swelling is induced by fast neutrons ( $E > 0.1$  MeV) which cause damage to the material. For the void swelling study, displacement per atom (dpa) is used to link ion irradiation and neutron irradiation for comparison purposes.

Therefore, in the rest of the paper, fast neutron doses will be converted into dpa, and the total fluence will be characterized by the ratio,  $r$ , of the thermal to the fast fluence. No explicit mention of the thermal dose will be expressed.

According to Farrell et al. [34], the conversion of fast neutrons ( $> 0.1$  MeV) to dpa is  $1.8 \cdot 10^{23} \text{ n.cm}^{-2} \equiv 260 \text{ dpa}$ . This value will be used in the rest of this paper.

##### 4.1 Quantification of the swelling from silicon

In order to quantify the contribution of silicon onto the swelling, data from the literature has to be considered. Only Farrell [35] published calculations of the silicon induced swelling. According to the graph reported in [35], the silicon induced swelling can be described by the following formula:

$$\left(\frac{\Delta V}{V}\right)_{Si} (\%) = 6.10^{-24} F_r$$



With  $F_r$  the fast neutron flux in  $\text{n.cm}^{-2}$ . However, it is the thermal neutron flux which leads to swelling due to transmutation. This data point is from the HFIR target holder for which the thermal ( $E < 0,625 \text{ eV}$ ) to fast ( $E > 0,1 \text{ MeV}$ ) neutrons ratio is equal to 2. The formula can therefore be written as:

$$\left(\frac{\Delta V}{V}\right)_{Si} (\%) = 3.10^{-24} F_{th}$$

Introducing the  $r$  ratio for any reactor:

$$\left(\frac{\Delta V}{V}\right)_{Si} (\%) = 3.10^{-24} F_r \cdot r$$

Acknowledging the previously written formula linking  $F_r$  to dpa:

$$\left(\frac{\Delta V}{V}\right)_{Si} (\%) = 3.10^{-24} \frac{1.8.10^{23}}{260} dpa \cdot r$$

The total dpa is the product of the damage rate  $K$  in  $\text{dpa.s}^{-1}$  with time  $t$  in s:

$$\left(\frac{\Delta V}{V}\right)_{Si} (\%) = 2.077.10^{-3} K \cdot t \cdot r$$

To convert the thermal flux ( $E < 0,625 \text{ eV}$ ) into conventional neutron flux, as there is no indication of this conversion ratio in [33], we re-calculated the contribution of precipitated silicon to swelling as a function of the conventional flux, using the cross section of 234,4 mbarns at  $E = 0,0254 \text{ eV}$  and  $T = 20^\circ\text{C}$  for neutron capture on  $^{27}\text{Al}$ . A good agreement with the silicon swelling line published in [33] was obtained for a  $F_{\text{conv}}/F_{\text{th}}$  ratio between 0.7 and 0.8. The  $F_{\text{conv}}/F_{\text{th}}$  ratio in the model will therefore be approximated to 0.7, which gives by dividing by 0.7 the final formula:

$$\left(\frac{\Delta V}{V}\right)_{Si} (\%) = 2.9671.10^{-3} K \cdot t \cdot r$$

Where  $r$  becomes the ratio  $F_{\text{conv}}/F_r$  ( $> 0,1 \text{ MeV}$ ).

#### 4.2 Swelling induced by voids

Measurements from S (single beam) and M (multiple beams) groups were performed on TEM pictures representing what is assumed to be a representative microstructure of the temper after irradiation. Swelling values are given assuming a 100 nm thickness. Raw data is given in the appendix A (page 35). For water and oil temper, each row corresponds to a mean value in a TEM sample. For air temper, in each irradiation condition, the different contributions to swelling are listed: the cavities aligned with defects, the local concentration of cavities (like observed in Figure 7.b and Figure 13) and the nanocavities in the whole matrix. The detailed formula for evaluation of the swelling using TEM pictures is given in the appendix B.

**Table 5: Mean swelling values for different conditions. Air temper values are the sum of the mean swelling value around defects and the value from nanocavities**

Temper	Conditions	$N_0$ ( $10^{20}$ voids.m <sup>-3</sup> )	Std. Dev.	$\frac{\Delta V}{V}$ (%)	Std. Dev.
Water	S-60	1.09	0.45	0.67	0.48
	S-100	5.31	1.56	0.46	0.29
Oil	S-60	2.82	1.35	0.37	0.13
Air	S-60			0.65	
	S-100			0.73	
	M-9			0.41	

Table 5 presents the summarized and averaged values of swelling from appendix A. Air temper values are obtained by summing the mean swelling near defects and the nanocavities. Values from local concentrations of irregular voids are not taken into account because of low number and random distribution which would distort the values given for a global swelling measurement.

First, it is observed that the standard deviation of the void swelling for S-100 and S-60 in water temper is extremely high, revealing the measurement difficulties due to the heterogeneous cavities distribution and to the high magnification necessary to observe the cavities. Moreover, S-60 presents a higher swelling than S-100, which is not expected. The medium number of cavities is clearly higher for S-100 than for the S-60 conditions (even when considering the standard deviation). This could be explained by the high energy of the Au ions (3.5 MeV) which seems to lead, at a high damage level, to smaller and more abundant cavities. Nevertheless, the high value of the S-100 sample could also be explained by the relatively small probed volume and the rapidly changing damage rate (0.4 dpa.nm<sup>-1</sup>).

Oil temper presents a higher void density and a lower swelling than water temper in the same conditions. However, standard deviations are overlapping. In air tempered specimens, higher values of swelling are observed. However, acknowledging they are obtained by summing different positions and origins of voids, no meaningful standard deviation values can be provided. Nevertheless, it is observed that even in M-9 conditions, a high swelling (0.41%) is already measured. As written in appendix A, swelling in air temper is mainly induced by nanocavities which form at low damage levels. The histograms presented in Figure 15 show the radius distribution of voids in air temper, depending on the source of the voids. It is observed that while aligned voids present a large distribution from a few nanometers to more than 60 nm, the radii of nanocavities do not exceed 6 nm.

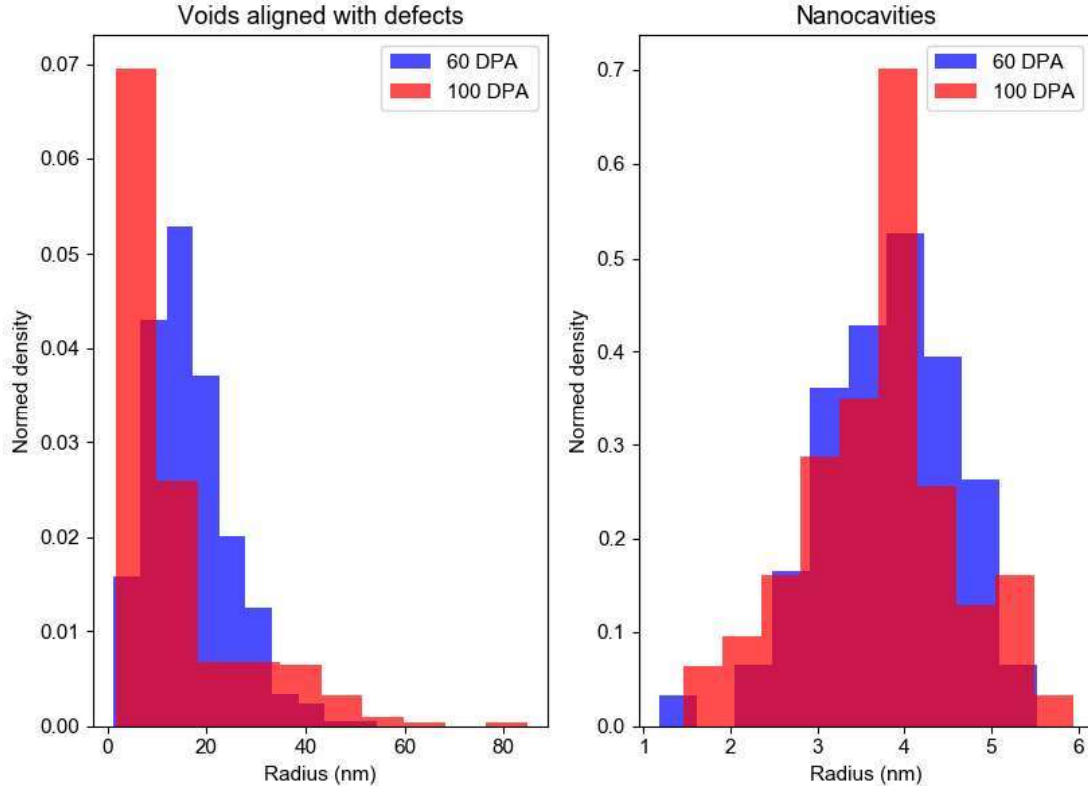


**Figure 15: Size distribution of void radius depending on the void types for S-60 and S-100 conditions in air temper.**

#### 4.3 Application to the Brailsford&Bullough model

Modeling the void swelling is a complex issue as it depends on various parameters which are usually not easily determined. Models found in the literature are also quite varied. Dai et al. promoted the critical bubble model (*CBM*) [4] which takes into account many parameters. However, current knowledge on the void swelling of aluminum alloys is not sufficient to feed such a complex model properly. On the other hand, simpler models like the Brailsford and Bullough model (*BBM*) [23,24] are enough to estimate the void swelling of aluminum core components in reactors. The BBM is written with three equations:

$$\frac{\Delta V}{V}(\%)(t) = SF(\eta)K\Delta t \quad 1$$

$$\eta = 400 \exp \left[ -\frac{E_m^v}{k} \left( \frac{1}{T_s} - \frac{1}{T} \right) \right] \quad 2$$

$$F(\eta) = \frac{2}{\eta} \left[ \sqrt{1 + \eta} - 1 - \frac{\eta}{2} \exp \left[ -\frac{Q}{k} \left( \frac{1}{T} - \frac{1}{T_t} \right) \right] \right] \quad 3$$

In equation 1,  $S$  is an adjusting parameter to make the model comply with experiments.  $K$  is the damage rate in  $\text{dpa.s}^{-1}$  and  $\Delta t$  the time variation from  $t_0$ , where  $t_0$  is the time at which the material begins to swell.  $F(\eta)$  function is described in equations 2 and 3. In equation 2 and 3,  $E_m^v$  is the activation energy for vacancy motion in eV and  $Q$  the activation energy for self-diffusion by the vacancy mechanism in eV.

T is the irradiation temperature in K.  $T_s$  is the low activation temperature under which the vacancy and interstitial motion is too low to form voids.  $T_t$  is the high limit temperature above which the recombination rate is so high that no void can be formed. k is the Boltzmann constant.

In the context of this study, determining a time at which the material begins to swell is not practical since this value depends on the damage rate. It is therefore more adapted to use  $\Phi_0$ , the dpa value at which the material begins to swell. The BBM is therefore written as:

$$\frac{\Delta V}{V}(\%) = SF(\eta)(Kt - \Phi_0)$$

Among the parameters to be determined, Q and  $E_m^v$  can be found in the literature. It will be assumed that  $E_m^v = 0.65$  eV [36] and  $Q = 1.31$  eV [37]. Concerning  $T_s$  and  $T_t$ , data from the literature are limited. Figure 16, reproduced from Jahnke et al. [8], presents swelling curves after irradiation with 100 keV  $Al^+$  ions as a function of temperature, at three different damage values, obtained with different dpa rates. Comparing blue, green and red curves obtained on pure aluminum shows that increasing the dpa rate raises the temperature of the swelling peak and therefore impacts  $T_s$  and  $T_t$ . Moreover, the neutron irradiations (black curve) present a different behavior than ion irradiated samples: the peak temperature is shifted toward lower temperatures, in relation with the lower damage rate actually obtained with neutrons. Furthermore, the peak temperature in an AlMgSi alloy is shifted towards lower temperatures when compared to pure aluminum, both irradiated with ions with the same damage rate. But the metallurgical state (orange curves) does not seem to have an impact on the peak temperature, but only on the swelling level. In [8] Jahnke points the variability of  $T_s$  and  $T_t$ , however no value for any 6000 aluminum alloy has been determined so far. Therefore, in order to model the swelling of aluminum alloys, estimations have to be done. Using parabolic curves to extrapolate Jahnke data concerning the AlMgSi alloy, it is proposed to estimate  $T_s = -20^\circ C$  and  $T_t = 210^\circ C$ .

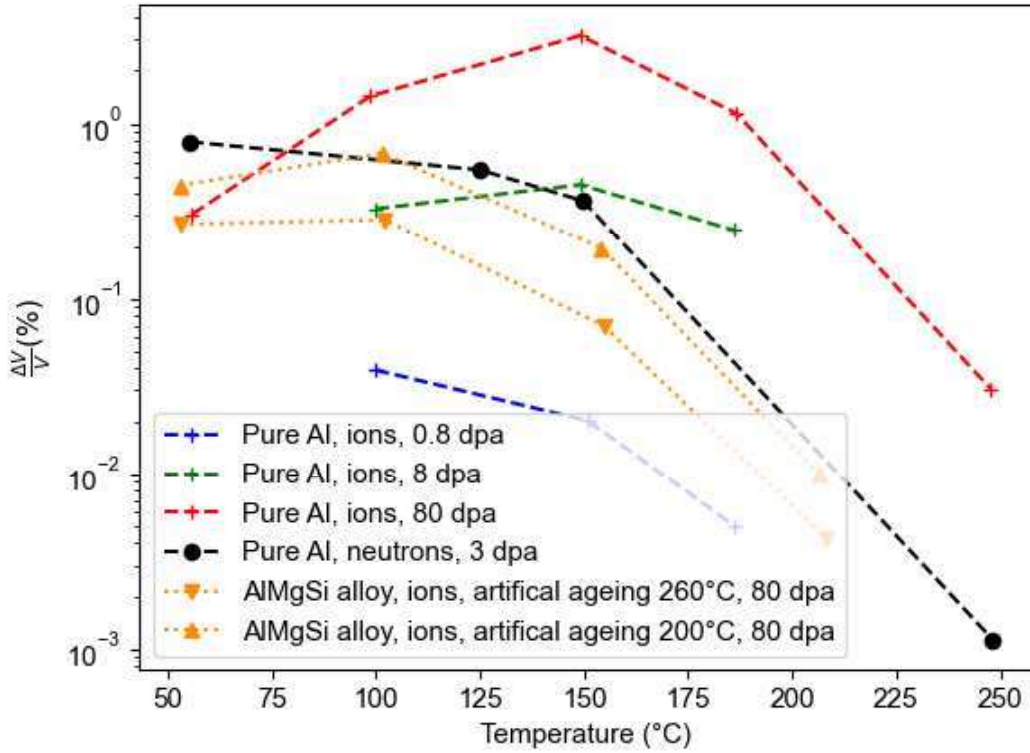


**Figure 16: Voids swelling for different alloys with different irradiation conditions vs temperature [8]**

$\Phi_0$  can be evaluated as the intersection between the swelling from silicon curve and the 6061-T6 global swelling in the Farrell experiments [35]. This calculation gives  $\Phi_0 = 41,8$  dpa. Considering the uncertainty on the slopes of the fitted lines, the  $\phi_0$  value for the modeling will be rounded to 40 dpa.

Figure 17 is a plot of all data on 6061-T6 retrieved from Farrell after neutron irradiations [35] and from experiments after ion irradiations presented in this paper. A high inhomogeneity is observed for our study using ion irradiation, and a decrease of swelling values with increasing dpa, which prevents the fitting of our data using the BBM model. According to Figure 17, the swelling values measured after neutron irradiations also present a high dispersion with three high values, two low values close to the silicon swelling line and one value at low dpa possibly fitting two different lines. This dispersion can be related to the different neutron spectra (r ratio) seen by the samples: at a given dpa, the contributions of the silicon swelling and of the void swelling can vary in a large range. Indeed, the silicon swelling is dependent on the r ratio, and the void swelling on the fast flux level, i.e. the damage rate.

That is why, two simulations will be performed, using two different damage rates: one fitting the high swelling values measured after neutron irradiations and the other adapted to the low swelling values. Figure 18 presents both BBM curves using damage rates of  $5 \cdot 10^{-7}$  and  $1 \cdot 10^{-6}$  dpa.s<sup>-1</sup>.

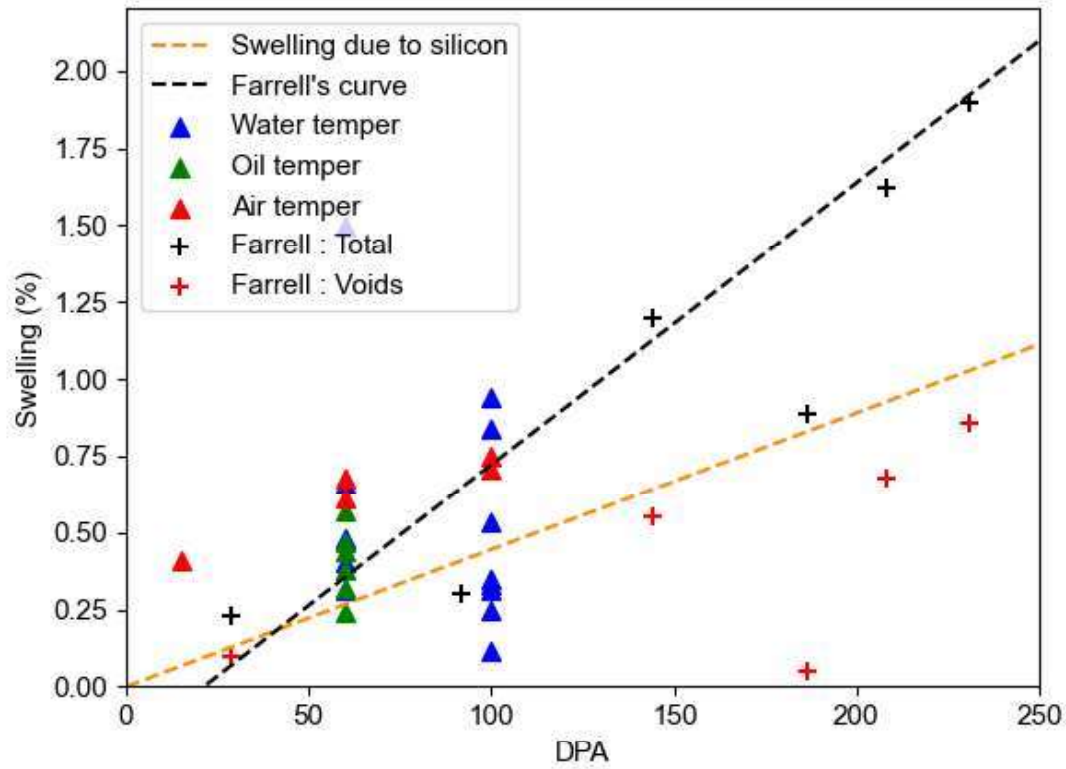


Figure 17: A global overview of swelling values. Crosses are values from Farrell experiments (neutrons). Triangles are values from this study (Au+ ions) with the color indicating the quench.

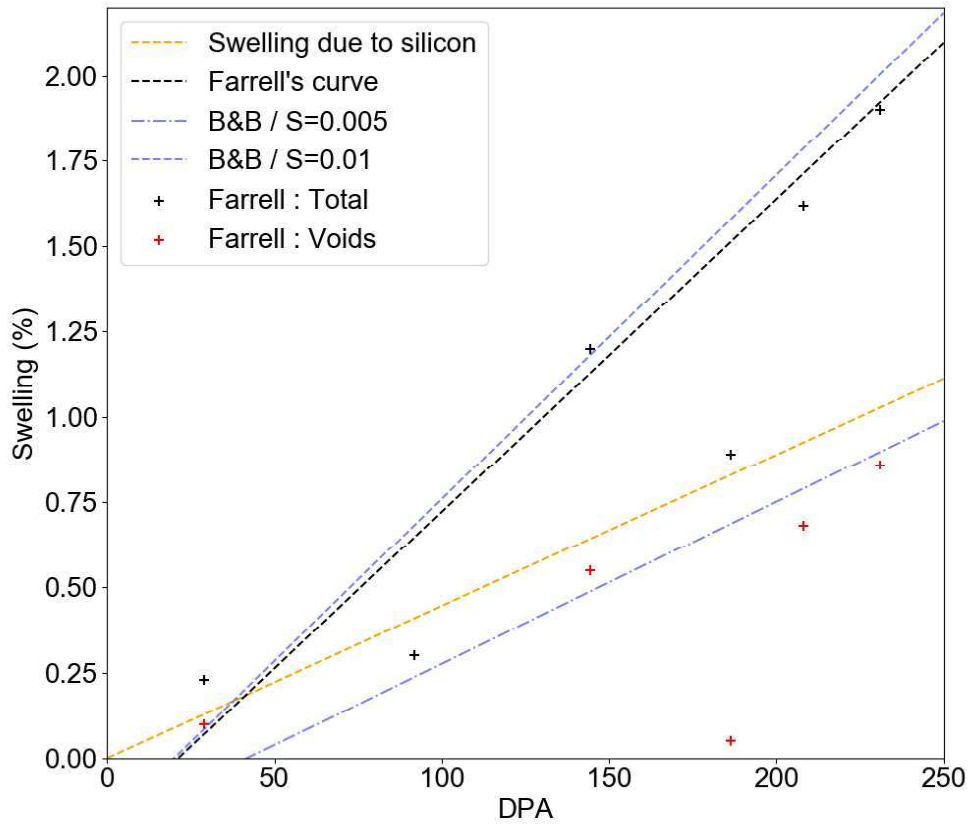
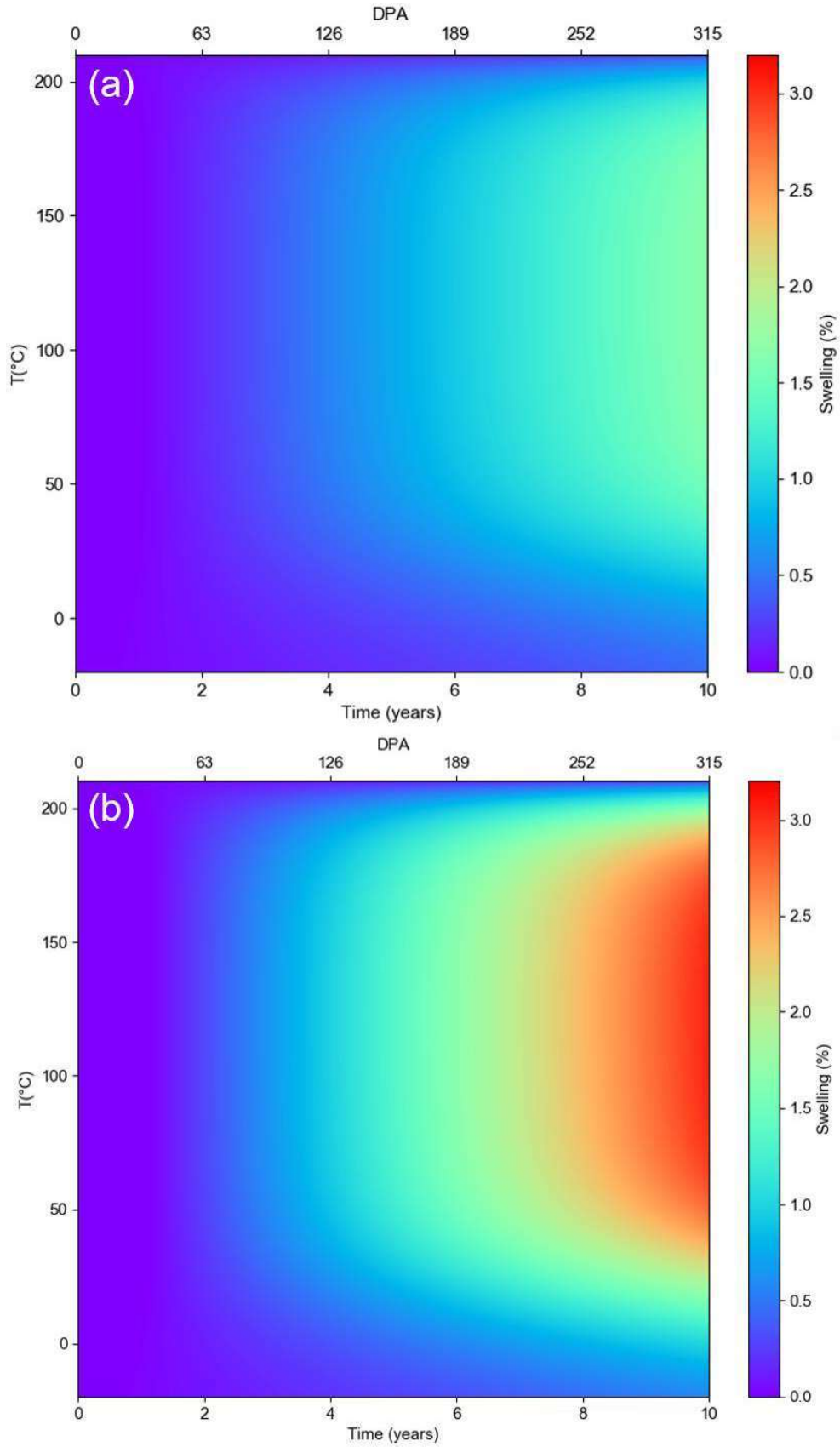
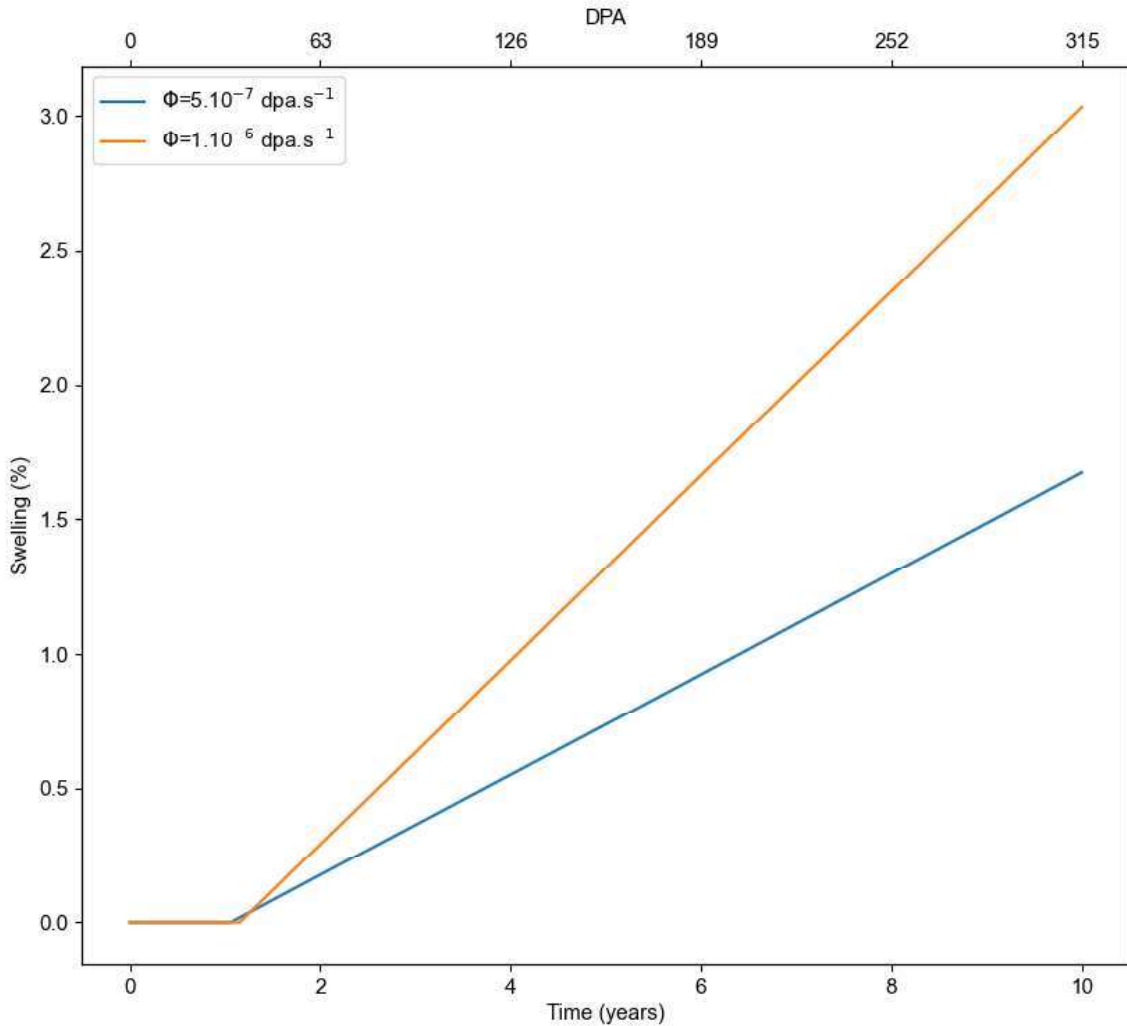


Figure 18: Adapted BBM for damage rates of  $1.10^{-6}$  and  $5.10^{-7}$  dpa.s<sup>-1</sup> with S=0,01



**Figure 19: Modelling of the total swelling (silicon + voids) of a 6061-T6 alloy under neutron irradiation during 10 years at 2 different values of the damage flux (a)  $5 \cdot 10^{-7} \text{ dpa.s}^{-1}$  ( $\sim 3.5 \cdot 10^{14} \text{ n.cm}^{-2} \cdot \text{s}^{-1}$ ,  $E > 0.1 \text{ MeV}$ ) (b)  $1 \cdot 10^{-6} \text{ dpa.s}^{-1}$  ( $\sim 6.9 \cdot 10^{14} \text{ n.cm}^{-2} \cdot \text{s}^{-1}$ ,  $E > 0.1 \text{ MeV}$ ) with a thermal to fast neutron ratio of 1/3 using a BBM coefficient  $S=0.01$ . Values are plotted for a temperature range of  $-20^{\circ}\text{C}$  to  $210^{\circ}\text{C}$**

Figure 19 shows the global swelling of a 6061-T6 component inside a reactor. This simulation is obtained with the BBM model and the swelling from silicon as calculated previously. It is calculated for a damage flux of  $1.10^{-6} \text{ dpa.s}^{-1}$  equivalent to about  $6.9.10^{14} \text{ n.cm}^{-2}.\text{s}^{-1}$  ( $E > 0,1 \text{ MeV}$ ) for the fast neutron flux, which is about the highest expected in a research reactor core and for a damage flux of  $5.10^{-7} \text{ dpa.s}^{-1}$  equivalent to a fast neutron flux of about  $3.5.10^{14} \text{ n.cm}^{-2}.\text{s}^{-1}$  ( $E > 0,1 \text{ MeV}$ ). The thermal to fast neutrons ratio chosen is  $r=1/3$ . The plot displays the estimated swelling for a temperature range between  $T_s$  and  $T_t$  for a period of time of 10 years. Figure 19.b pictures the swelling at the maximal damage flux of  $1.10^{-6} \text{ dpa.s}^{-1}$  and Figure 19.a the swelling at half this value. Concerning the temperatures themselves,  $90^\circ\text{C}$  is representative of a high temperature reached in a NRR core. Figure 20 displays the swelling at  $90^\circ\text{C}$  during the same period of time. For a damage flux of  $5.10^{-7} \text{ dpa.s}^{-1}$ , a final swelling of 1.7% is expected. In the case of a maximal damage flux of  $1.10^{-6} \text{ dpa.s}^{-1}$ , 3.0% is obtained.



**Figure 20: Modelling of the total swelling (silicon + voids) of a 6061-T6 alloy under neutron irradiation during 10 years at 2 different values of the damage flux:  $1.10^{-6} \text{ dpa.s}^{-1}$  ( $\sim 6.9.10^{14} \text{ n.cm}^{-2}.\text{s}^{-1}$ ,  $E > 0.1 \text{ MeV}$ ) and  $5.10^{-7} \text{ dpa.s}^{-1}$  ( $\sim 3.5.10^{14} \text{ n.cm}^{-2}.\text{s}^{-1}$ ) with a thermal to fast neutron ratio of 1/3 using a BBM coefficient  $S=0.01$  at  $90^\circ\text{C}$**



## 5 Discussion

Because of the variety of results reported in the present study, in the following discussion, microstructure observations have to be considered separately from the modeling. Also in order to understand the role of helium and silicon implantation, results from S and T conditions must be considered and commented separately.

### 5.1 Microstructural modifications

#### 5.1.1 Single beam irradiation

Single beam irradiation conditions have revealed the response of the microstructure under irradiation. First, as presented Figure 1, dispersoids are totally amorphized by irradiation and, depending on their nature and on the damage level, partially or totally dissolved. This is observed for all temper. In the case of oil tempered specimens, heterogeneous precipitation, present before irradiation is not observed after. Similarly, in air temper, where very coarse and heterogeneous particles (oxides) were observed before irradiation, they were not observed after. At low dpa, these coarse particles are observed to be dissolved (Figure 7). These results show that heterogeneous precipitates are totally dissolved during irradiation while  $\alpha$ -Al(Mn,Fe)Cr dispersoids are more stable only showing a partial dissolution and an amorphization. Amorphization of the microstructure and modification in the dispersoids near environment have been already observed in the same family of materials during ion irradiations [38]. A lower quenching rate implies a higher heterogeneity in the submicronic precipitation, which induces a lower stability of the precipitation during irradiation.

At the nanometric scale, precipitates have been observed with APT for the low dpa irradiation (Figure 4) and by TEM at the high dpa ones. The presence of zinc in the nanoprecipitates detected by APT seem to indicate a migration of the zinc in solid solution toward the nanoprecipitates, which can be an early stage in the formation of new nanoprecipitates during irradiation. Indeed, Flament et al. showed by HRTEM observations that partial dissolution of the nanoprecipitates can occur and lead to the formation of new nanoprecipitates under ion irradiation [33]. While achieving roughly the same damage levels, these new precipitates are not observed in our study, which could result from the irradiation conditions and of the TEM resolution. Moreover, irradiation of aluminum alloys under neutron flux confirmed that the dissolution of nanoprecipitates occurs in reactors [39,40] ; however, 6000 aluminum alloys are known to keep good mechanical properties even after irradiation [34,41]. It is therefore highly likely that the dissolution-precipitation phenomena happen during neutron irradiations.

Concerning the void swelling mechanisms, different nucleation sites are observed. Figure 2 pictures many aligned cavities in the whole matrix. This observation of aligned cavities is assumed to be the signature of defects such as dislocations, grain boundaries or sub grain boundaries which, by being interstitial wells, induce the formation of cavities in their nearby environment. This is observed for all

tempers. Other cavities are also observed in the immediate surroundings of dispersoids for all tempers (Figure 3). Considering the fact that those particles are dissolving under irradiation, this means they are a preferred site of void formation. Moreover, in the oil and air temper, another types of cavities is observed. As seen Figure 5, cavities distant from dispersoids and showing no particular alignment are present. It is assumed that the dissolution of heterogeneous submicronic particles leads to the formation of interstitial wells which helped form such cavities. It is particularly clear for the air temper samples, in which local and extremely dense formation of voids (Figure 7.b) seems to be the results of a fast dissolution of submicronic particles. Previous studies on those particles [19] proved most of them to be oxides, which are known to be extremely fragile under irradiation. It is therefore conceivable that such a heterogeneous precipitation favors the formation of coarse cavities.

Finally, in air temper, a homogeneous distribution of nanoscale voids was observed in the whole matrix (Figure 6). Air temper is the only temper without nanoprecipitates. Therefore, as nanoprecipitation is semi-coherent, it plays the role of ambivalent wells, accommodating the microstructure and preventing the formation of voids. As air temper is devoid of nanoprecipitates, cavities are forming in the whole matrix.

Flament et al., observed cavities in the nearby environment of dispersoids [38]. Under neutron flux, studies on reactor elements showed a wide range of swelling measures and a void formation highly dependent on the alloy and the irradiation conditions [21,42–44]. However, Risbet et al. [45–47] studied the formation of voids in pure aluminum and model alloys under neutron flux. They demonstrate the role of defects in the formation of aligned voids, as observed in this study. The behavior of 6000 aluminum alloys under irradiation seems to be specific due to the various precipitation scales. According to Risbet et al. on 2000 aluminum alloys [45,47] and confirmed by the present study on 6000 alloys, the void swelling seems specifically localized on the submicronic precipitation and on pre-irradiation defects at the submicronic scale. Hence, pre-irradiation defects and coarse dispersoids are factors which promote the formation of voids in the alloys.

### *5.1.2 Triple beam irradiations*

The microstructure modifications after triple beam irradiations are notably different from those observed after single beam irradiation. Nano-bubbles are observed in the whole matrix for all tempers as seen Figure 9, Figure 10 and Figure 12. The EELS analysis, Figure 9, reveals helium inside the and a statistical analysis shows the bubbles size is directly linked to the amount of helium injected. In the vicinity of the dispersoids present in the matrix, bubbles tend to be rare and coarse (Figure 11). By comparison, after single beam irradiations, voids are not observed to be homogeneously distributed and preferential nucleation sites have been evidenced as reported by Farrell [21] who demonstrated that the helium production under neutron flux leads to an homogeneous dispersion of bubbles in the whole matrix. This was also observed in this study under ion beam.

1 The overall density of nanoprecipitates tends to decrease under irradiation while new ones form. This  
2 observation is likely to be linked to silicon implantation. According to Weeks et al. [48], the formation  
3 of silicon during neutron irradiation leads to the formation of silicon nano-precipitates.  
4

5 For the study of void swelling, the initial microstructure differences at the submicronic scale is not a key  
6 parameter since after helium implantation bubbles nucleate homogeneously in the matrix. Therefore,  
7 helium implantation tends to homogenize the formation of voids whatever the quenching rate. This  
8 seems to be beneficial for low quench rate where coarse voids are no longer observed in the place of  
9 previously present particles. But for high quench rates, it seems to produce numerous bubbles and  
10 homogeneously dispersed voids in the matrix which were not observed after single beam irradiations.  
11  
12  
13  
14  
15

## 16 *5.2 Modeling the swelling*

### 17 *5.2.1 Swelling data*

18 The calculation of the swelling inside TEM samples after single beam irradiation revealed extremely  
19 dispersed values. Water and oil temper samples had a very similar behavior in terms of swelling while  
20 the air temper showed higher values. Cavities from air temper seemed mostly consisting homogeneously  
21 distributed whereas water temper presented the most dispersed cavities as seen in Figure 17. These  
22 assessments show the high difficulty of evaluating a phenomenon like swelling in the aluminum alloys  
23 showing heterogeneous and homogenous formation of cavities at various scale. Due to the variety of  
24 nucleation sites for the voids and bubbles, estimating the nucleation the most representative site for  
25 global swelling is not obvious. For that matter, the similar values measured for different irradiation  
26 conditions in the air temper can be attributed to the fact that the major contributors to the swelling in  
27 this temper are the nanovoids present in the entire matrix. As this contribution is homogeneous and  
28 easily measurable, measurements in the air temper can allow us to estimate the swelling for these  
29 conditions.  
30  
31  
32  
33  
34  
35  
36  
37  
38  
39  
40

41 More, aluminum alloys are seen to be extremely sensitive to the thermal treatment as seen on Figure 16  
42 and the previous section. Therefore, as the exact tempering and composition of the 6061 alloy used in  
43 Farrell [35] is unknown and unlikely to be the same as used in this study it is highly probable that these  
44 different parameters partially explain the difference between the two curves. In addition, the high  
45 dispersion between the measurements in water temper for 100 dpa (Figure 17) pictures the issue of  
46 working with heavy ions as the very high damage rate inside the depth (around 100 dpa every 450 nm,  
47 Figure A.1) implies difficulties on the measurement of a homogeneous swelling inside such specimens.  
48  
49  
50  
51  
52

### 53 *5.2.2 Model and parameters*

54 The BBM model was chosen in this study to evaluate the swelling in a typical NRR after 10 years of  
55 irradiation. It is obvious that more recent and more physical models like the CBM outperforms the BBM.  
56 However, in the current state of art on the swelling of aluminum alloys, some of the CBM inputs are  
57  
58  
59  
60  
61  
62  
63  
64  
65

still unknown. First,  $T_s$ ,  $T_t$  and  $\Phi_0$  were chosen from raw literature data. As observed in Figure 16,  $T_s$  and  $T_t$  are mainly influenced by the material composition and by the damage rate. Indeed, the reduction of the swelling peak temperature at low damage rates for pure aluminum is observed. Second, microstructures resulting from different thermal treatments obviously modify the swelling level but according to [8] not the temperature range. In this study on 6061-T6 alloy,  $T_s$  and  $T_t$  were evaluated using previous data on an AlMgSi model alloy which has a close chemical composition, and which was irradiated with  $Al^+$  ions at a comparable damage level. However, a different temperature range should be taken for modeling neutron irradiations on 6061, but no data is available. The real values of  $T_s$  and  $T_t$  remain unknown due to the important dispersion of the T6 tempers microstructures before irradiation. In addition, the chosen value of  $\Phi_0$  is based on swelling measurements of 6061-T6 alloy after neutron irradiations, whereas  $\Phi_0$  is highly dependent on the damage flux. As two different damage rates were considered in the model, two different values should be adopted for  $\Phi_0$ , but the poor number of swelling data under neutron flux did not allow to do it.

### 5.2.3 Swelling values obtained from the model

Final results presented Figure 19 show an increase of the swelling with the damage level and a swelling peak around 110°C. For 10 years inside reactors under high fast neutron flux, the range of results (1.7% to 3%) seems reasonable. The difference between both results lies in the large range of damage fluxes in a research reactor, depending on the location in the core.

The larger swelling values measured after ion irradiation in our study can be attributed to the higher damage rates obtained with ions. The difference in terms of damage rates ( $1.10^{-6}$  dpa.s<sup>-1</sup> for the highest neutron fluxes to  $1.10^{-4}$  dpa.s<sup>-1</sup> on average for ions) modifies the swelling kinetics itself. Increasing the damage rate reduces the probability of recombining interstitials and vacancies and therefore increases the swelling. Furthermore, in nuclear reactors, transition periods, stops, reboots, thermal fluxes and neutron flux variations modify and globally lower the swelling compared to ion irradiations performed in one batch. In addition, the chosen high flux and fluence in our ion irradiations lead to a wide damage range (150-400 dpa) in a short thickness (1 μm) which introduces an uncertainty in the determination of a swelling associated to a damage level. Finally, it has been demonstrated earlier in this study that the metallurgical state is conditioning the voids sizes and distribution. Yet the precise metallurgical state of the components in 6061-T6 alloy assessed by Farrell [21,34,35] is unknown and therefore the comparison between ion and neutron irradiations is impacted by probable differences in the quenching rate, added to chemical composition variations.

## 6. Conclusion and perspectives

This study demonstrates the impact of the metallurgical state on the swelling of aluminum alloys. 6000 aluminum alloys are widely used in NRRs and show a very wide range of microstructures resulting from the thermal treatment of the thick plate representative of the NRR component material. While the annealing and artificial ageing are well mastered in the nuclear industry, the impact of quenching still remains poorly documented.

It has been shown that the void swelling of 6061 aluminum alloy depends on the quenching rate. The coarse submicronic particles which precipitate in the alloy mostly at low cooling rates dissolve quickly under irradiation, causing an early formation of voids. While  $10^{\circ}\text{C.s}^{-1}$  is regarded as the average critical quenching rate used as a criterion for the mechanical properties of a T6 temper on 6000 alloys, it should be noted that it was established on thin plates and inherited from the automotive industry in which irradiation issues are absent. This study shows that for applications using thick components, such as the nuclear industry, the highest cooling rates have to be targeted in order to avoid the nucleation of coarse submicronic phases and to increase as much as possible the precipitation of hardening phases which not only harden the alloy but limit the formation of voids during irradiation.

A Brailsford and Bullough model (BBM) has been used to simulate the swelling of 6061-T6 alloy under neutron irradiation and adjusted on published values. The lack of knowledge on some parameters specific to the swelling in 6061-T6 alloy is an important point. In particular, the threshold damage  $\Phi_0$  over which void swelling occurs is derived from neutron irradiations data, but its dependence on the damage rate should be investigated. In addition, the temperature range corresponding to swelling of 6061-T6 alloy is derived from published ion irradiation data, but data on pure aluminum show that the temperature of maximal swelling is lower with neutron than with ion irradiations. Swelling data on NRR components irradiated at different temperatures should allow the determination of  $T_s$  and  $T_t$  more accurately and their dependence on the grading and the damage rate. A global understanding of the variation of those parameters is of primary interest to achieve a more correct simulation with BBM. Finally, it has to be reminded that achieving a better BBM modeling is only the first step leading to the use of more complex irradiation model like the CBM.

The comparison of results after neutron and ion irradiations reveals that the void swelling from ion irradiations presents a very high dispersion and overestimates the global swelling on most samples. A part of the dispersion can be explained by the uncertainty in correlating the observed area with a damage rate. But another part of the dispersion is intrinsic to the alloy which presents a heterogeneous swelling linked to the local microstructure at the nanoscale. The very high damage rate in ion irradiations explains the overestimation of the void swelling for most samples. This is why ion irradiations should be made at a reduced flux even at the cost of a longer irradiation time to achieve high damage levels, in order to obtain results more representative of a neutron irradiation.

1 Ultimately, it is pointed out that core components that are generally thicker than pieces used in the  
2 automotive industry need additional dedicated microstructural and irradiation studies. Acknowledging  
3 that different cooling rates imply different swelling behaviors, it is of primary interest to dispose of a  
4 swelling model allowing to predict the swelling of a thick 6061-T6 specimen presenting different  
5 cooling rates in the thickness.  
6  
7

## 8 9 **Acknowledgments**

10 This work received assistance from the “Agence Nationale de la Recherche” program GENESIS  
11 referenced as ANR-11-EQPX-0020. The author also wants to thank the French Atomic Energy  
12 Commission (CEA) for funding this study. A very special thanks is addressed to the JANNuS team for  
13 the extraordinary work and dedication in the making of the presented irradiation experiments.  
14  
15  
16  
17  
18  
19  
20  
21  
22  
23  
24  
25  
26  
27  
28  
29  
30  
31  
32  
33  
34  
35  
36  
37  
38  
39  
40  
41  
42  
43  
44  
45  
46  
47  
48  
49  
50  
51  
52  
53  
54  
55  
56  
57  
58  
59  
60  
61  
62  
63  
64  
65

# **Appendix A: Voids swelling values from ion irradiations S and M**

## *A.1: Water temper*

Conditions	$N_0$ ( $10^{20}$ voids.m <sup>-3</sup> )	$\frac{\Delta V}{V}$ (%)
<b>S-100</b>	5.20	0.33
	7.40	0.94
	6.00	0.31
	4.60	0.25
	4.80	0.12
	5.80	0.53
	2.20	0.35
	6.50	0.84
<b>S-60</b>	0.90	0.48
	1.80	1.50
	0.78	0.31
	0.71	0.66
	1.30	0.40
<b>M-9</b>	<i>No voids observed</i>	

## *A.2: Oil temper*

Conditions	$N_0$ ( $10^{20}$ voids.m <sup>-3</sup> )	$\frac{\Delta V}{V}$ (%)
<b>S-60</b>	2.06	0.38
	3.04	0.24
	1.17	0.44
	2.45	0.32
	5.17	0.57
	4.21	0.47
<b>M-9</b>	<i>No voids observed</i>	

A.3: Air temper

Conditions	Source	N <sub>0</sub> (10 <sup>20</sup> voids.m <sup>-3</sup> )	$\frac{\Delta V}{V}$ (%)
<b>S-100</b>	<i>Defects</i>	1.05	0.14
	<i>Defects</i>	1.34	0.18
	<i>Heaps</i>	21.5	5.67
	<i>Heaps</i>	11.1	12.9
	<i>Heaps</i>	25.3	4.48
	<i>Nanocavities</i>	190	0.57
<b>S-60</b>	<i>Defects</i>	1.21	0.17
	<i>Defects</i>	2.09	0.24
	<i>Heaps</i>	15.6	6.24
	<i>Nanocavities</i>	186	0.44
<b>M-9</b>	<i>Defects</i>	<i>No voids observed</i>	
	<i>Heaps</i>	<i>No voids observed</i>	
	<i>Nanocavities</i>	112	0.41



## Appendix B: Calculation of the voids swelling using TEM pictures

According to Jahnke [8,49], the voids swelling in an observed area in TEM is given by :

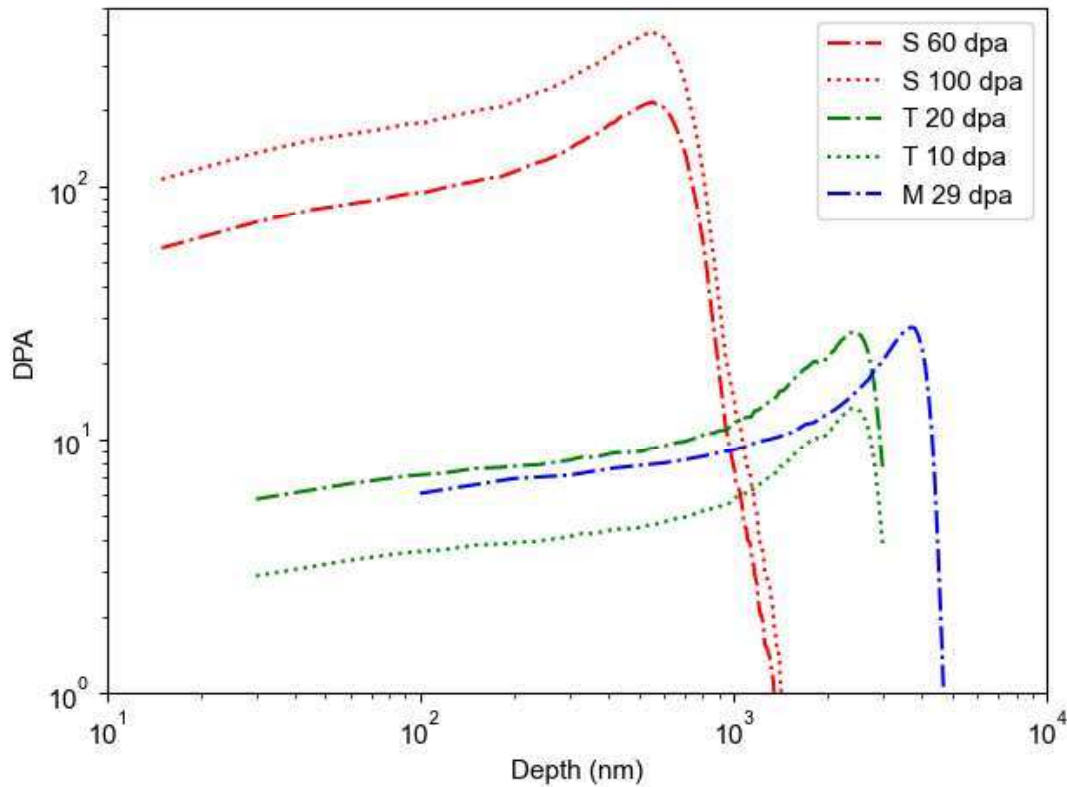
$$\left(\frac{\Delta V}{V}\right)_{void} (\%) = 100 \frac{\sum V_c}{V_z}$$

With  $V_c$ , the volume of a given void and  $V_z$  the total volume of the observed area. Assuming a thickness of 100 nm in this area and voids to be spherical, it can be written that:

$$\left(\frac{\Delta V}{V}\right)_{voids} (\%) = 100 \frac{4}{3} \pi \frac{\sum R_c^3}{S_z * 100}$$

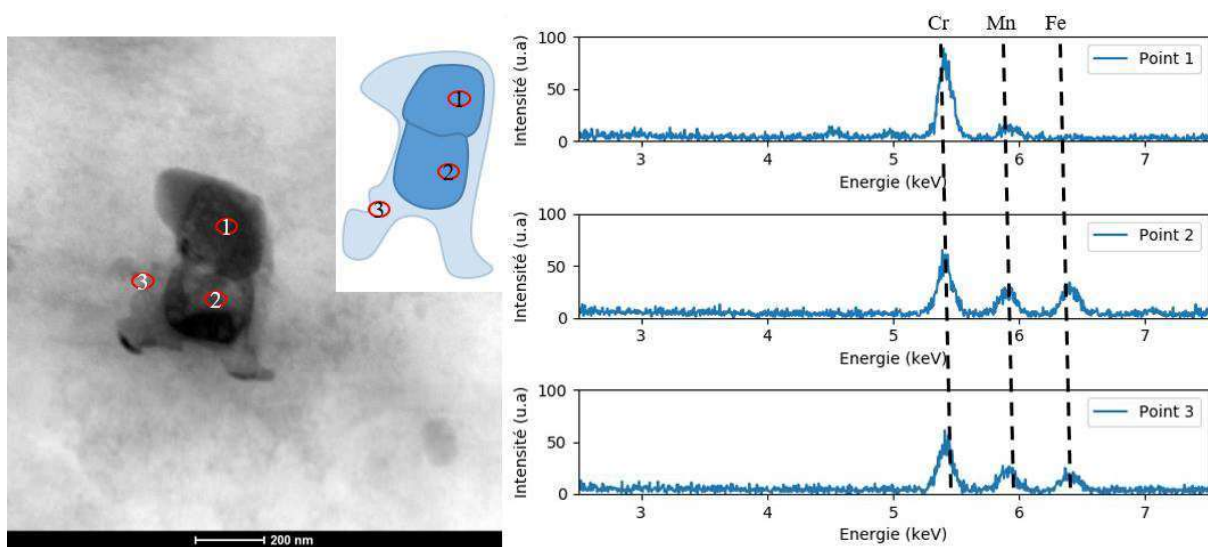
With  $R_c$  the radius of the void in nm and  $S_z$  the surface of the picture in nm<sup>2</sup>.

## Appendix C: Supplementary material



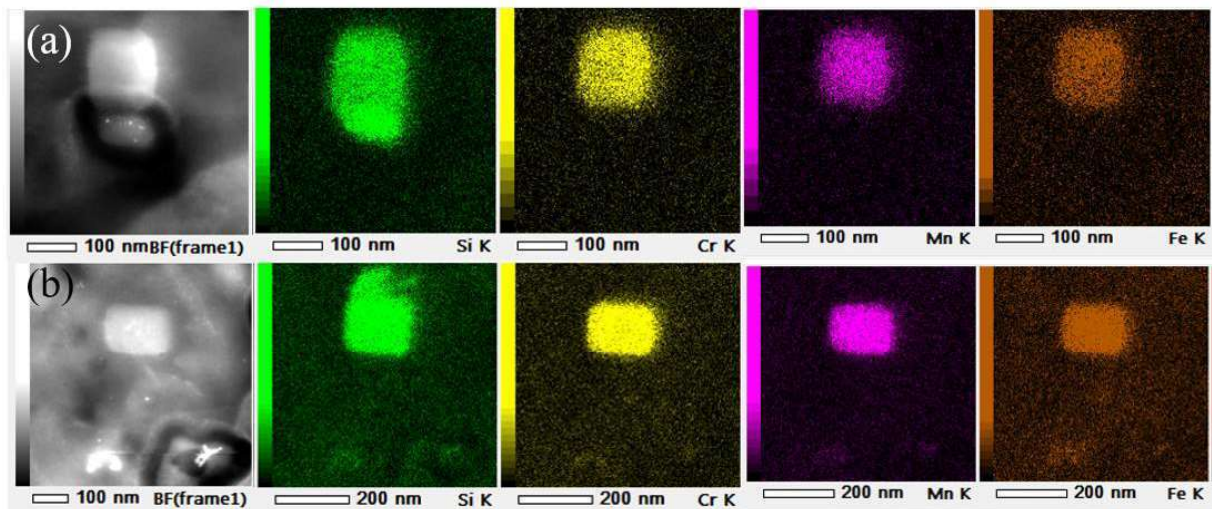
**Figure A.1:** Damage profile simulated by SRIM for each group and targeted dpa. Curves are corrected by the real fluence measured at the end of the irradiation experiments.

Figure A.1 shows the irradiation profiles obtained using SRIM.



**Figure A.2:**  $\alpha$ -type particle observed after irradiation in a S-60 irradiation. EDS points (1,2,3) were performed and related spectra is given.

Figure A.2 shows submicronic particles observed in single beam ion irradiated water temper samples. The two particles are surrounded by a diffuse aspect area. EDS analysis has been carried out in the two particles (points 1 and 2) and in the diffuse area (point 3). EDS experiments in point 1 revealed a high chromium and manganese amount with a lack of iron. Point 2 pictured important levels from the three elements Cr, Mn, Fe, whereas point 3 presented smaller concentrations of the same elements. This is consistent with a depletion in Fe of the alpha phase dispersoid particles observed before irradiation [50].



**Figure A.3: EDS analysis near dispersoids after S-60 irradiation conditions: most of heterogeneously disturbed species have vanished**

Figure A.3 pictures an EDS analysis on dispersoids in the oil temper before (a) and after (b) S-60 irradiation. The silicon particle in contact with the dispersoid has been dissolved during irradiation, whereas the dispersoid displayed only a partial dissolution and the remaining reduced dispersoid appeared to be denser. But, as the silicon solubility is low, a high silicon concentration is still observed around the dispersoid. These results show that the ion irradiation tends to erase the heterogeneous precipitation where smaller dispersoids present a homogeneous partition of elements.

## References

- [1] G.S. Was, Z. Jiao, E. Getto, K. Sun, A.M. Monterrosa, S.A. Maloy, O. Anderoglu, B.H. Sencer, M. Hackett, Emulation of reactor irradiation damage using ion beams, *Scr. Mater.* 88 (2014) 33–36. <https://doi.org/10.1016/j.scriptamat.2014.06.003>.
- [2] G.R. Odette, Modeling of microstructural evolution under irradiation, *J. Nucl. Mater.* 85–86 (1979) 533–545. [https://doi.org/10.1016/0022-3115\(79\)90542-7](https://doi.org/10.1016/0022-3115(79)90542-7).
- [3] C. Lemaignan, Nuclear Materials and Irradiation Effects, *Handb. Nucl. Eng.* (2010) 543–642. [https://doi.org/10.1007/978-0-387-98149-9\\_6](https://doi.org/10.1007/978-0-387-98149-9_6).
- [4] Y. Dai, G.R. Odette, T. Yamamoto, 1.06 - The Effects of Helium in Irradiated Structural Alloys, in: R.J.M. Konings (Ed.), *Compr. Nucl. Mater.*, Elsevier, Oxford, 2012: pp. 141–193. <https://doi.org/10.1016/B978-0-08-056033-5.00006-9>.
- [5] L.K. Mansur, Void Swelling in Metals and Alloys Under Irradiation: An Assessment of the Theory, *Nucl. Technol.* 40 (1978) 5–34. <https://doi.org/dx.doi.org/10.13182/NT78-2>.
- [6] M.B. Toloczko, F.A. Garner, V.N. Voyevodin, V.V. Bryk, O.V. Borodin, V.V. Mel'nychenko, A.S. Kalchenko, Ion-induced swelling of {ODS} ferritic alloy {MA957} tubing to 500 dpa, *J. Nucl. Mater.* 453 (2014) 323–333. <http://dx.doi.org/10.1016/j.jnucmat.2014.06.011>.
- [7] B.N. Singh, T. Leffers, M. Victoria, W.V. Green, D. Gavillet, Effects of 600 MeV proton irradiation on nucleation and growth of precipitates and helium bubbles in a high-purity Al-Mg-Si alloy, *J. Nucl. Mater.* 141 (1986) 743–747. [https://doi.org/10.1016/0022-3115\(86\)90084-X](https://doi.org/10.1016/0022-3115(86)90084-X).
- [8] B. Jahnke, K. Ehrlich, Void formation in an Al-Mg-Si alloy under different precipitation conditions after irradiation with 100keV Al ions, *J. Mater. Sci.* 15 (1980) 831–838.
- [9] G.E. Totten, D.S. MacKenzie, *Handbook of Aluminum: Vol. 1: Physical Metallurgy and Processes*, CRC Press, 2003.
- [10] K.R. Williams, S.B. Fisher, The void swelling of a  $\gamma'$ -hardened alloy, *Radiat. Eff.* 15 (1972) 243–250. <https://doi.org/10.1080/00337577208234699>.
- [11] R.R. Ambriz, D. Chicot, N. Benseddiq, G. Mesmacque, S.D. de la Torre, Local mechanical properties of the 6061-T6 aluminium weld using micro-traction and instrumented indentation, *Eur. J. Mech. - A Solids* 30 (2011) 307–315. <http://dx.doi.org/10.1016/j.euromechsol.2010.12.007>.
- [12] V. Fallah, B. Langelier, N. Ofori-Opoku, B. Raeisinia, N. Provatas, S. Esmaili, Cluster evolution mechanisms during aging in Al–Mg–Si alloys, *Acta Mater.* 103 (2016) 290–300. <https://doi.org/10.1016/j.actamat.2015.09.027>.
- [13] J. M. Gomez de Salazar, M. I. Barrena, The influence of Si and Mg rich phases on the mechanical properties of 6061 Al-matrix composites reinforced with Al<sub>2</sub>O<sub>3</sub>, *J. Mater. Sci.* 37 (2002) 1497–1502.
- [14] D. Maisonnnette, M. Suery, D. Nelias, P. Chaudet, T. Epicier, Effects of heat treatments on the microstructure and mechanical properties of a 6061 aluminium alloy, *Mater. Sci. Eng. A* 528 (2011) 2718–2724. <http://dx.doi.org/10.1016/j.msea.2010.12.011>.
- [15] J.L. Cavazos, R. Colás, Quench sensitivity of a heat treatable aluminum alloy, *Mater. Sci. Eng. A* 363 (2003) 171–178. [http://dx.doi.org/10.1016/S0921-5093\(03\)00616-6](http://dx.doi.org/10.1016/S0921-5093(03)00616-6).
- [16] A. Deschamps, Y. Bréchet, Influence of quench and heating rates on the ageing response of an Al–Zn–Mg–(Zr) alloy, *Mater. Sci. Eng. A* 251 (1998) 200–207. [https://doi.org/10.1016/S0921-5093\(98\)00615-7](https://doi.org/10.1016/S0921-5093(98)00615-7).
- [17] Fink & Willey, Quenching of 75S Aluminum Alloy, *Trans AIME* 175 (1947) 414–427.
- [18] J.L. Cavazos, R. Colás, Precipitation in a heat-treatable aluminum alloy cooled at different rates, *Mater. Charact.* 47 (2001) 175–179. [http://dx.doi.org/10.1016/S1044-5803\(01\)00164-4](http://dx.doi.org/10.1016/S1044-5803(01)00164-4).
- [19] V. Garric, K. Colas, P. Donnadieu, G. Renou, S. Urvoy, B. Kapusta, Correlation between quenching rate, mechanical properties and microstructure in thick sections of AlMgSi(Cu) alloys, *Mater. Sci. Eng. A* 753 (2019) 253–261. <https://doi.org/10.1016/j.msea.2019.03.045>.
- [20] K. Farrell, J.O. Stiegler, R.E. Gehlbach, Transmuted produced silicon precipitates in Irradiated Aluminium, *Metallography* 3 (1970) 275–284.
- [21] K. Farrell, Effects of structural imperfections on voids in aluminium – Microstructure impurity effects on void formation characteristics in neutron irradiated aluminium, Oak Ridge National Lab., 1971.

- [22] K. Farrell, Transmutation-produced silicon precipitates in irradiated aluminum, *Metallography*. 1970 (1970) 275–284. [https://doi.org/10.1016/0026-0800\(70\)90015-7](https://doi.org/10.1016/0026-0800(70)90015-7).
- [23] Brailsford A. D., Bullough Ronald, Marshall Walter Charles, The theory of sink strengths, *Philos. Trans. R. Soc. Lond. Ser. Math. Phys. Sci.* 302 (1981) 87–137. <https://doi.org/10.1098/rsta.1981.0158>.
- [24] A.D. Brailsford, R. Bullough, The rate theory of swelling due to void growth in irradiated metals, *J. Nucl. Mater.* 44 (1972) 121–135. [https://doi.org/10.1016/0022-3115\(72\)90091-8](https://doi.org/10.1016/0022-3115(72)90091-8).
- [25] V. Garric, Etude du gonflement par cavités d'un alliage d'aluminium irradié sous faisceau d'ions, Université Grenoble-Alpes, 2019.
- [26] Y. Serruys, P. Trocellier, S. Miro, E. Bordas, M.O. Ruault, O. Kaïtasov, S. Henry, O. Leseigneur, Th. Bonnaillie, S. Pellegrino, S. Vaubailon, D. Uriot, JANNUS: A multi-irradiation platform for experimental validation at the scale of the atomistic modelling, *J. Nucl. Mater.* 386–388 (2009) 967–970. <https://doi.org/10.1016/j.jnucmat.2008.12.262>.
- [27] J.F. Ziegler, M.D. Ziegler, J.P. Biersack, SRIM - The stopping and range of ions in matter (2010), *Nucl. Instrum. Methods Phys. Res. B.* 268 (2010) 1818–1823. <https://doi.org/10.1016/j.nimb.2010.02.091>.
- [28] V. Garric, A python alternative to SRIM, 2018. <https://github.com/victorgarric/pysrim> (accessed March 4, 2019).
- [29] C. Ostrouchov, costrouc/python-srim-implementation, 2019. <https://github.com/costrouc/python-srim-implementation> (accessed September 9, 2019).
- [30] L. Ding, Z. Jia, Z. Zhang, R.E. Sanders, Q. Liu, G. Yang, The natural aging and precipitation hardening behaviour of Al-Mg-Si-Cu alloys with different Mg/Si ratios and Cu additions, *Mater. Sci. Eng. A.* 627 (2015) 119–126. <https://doi.org/10.1016/j.msea.2014.12.086>.
- [31] P. Schumacher, S. Pogatscher, M.J. Starink, C. Schick, V. Mohles, B. Milkereit, Quench-induced precipitates in Al-Si alloys: Calorimetric determination of solute content and characterisation of microstructure, *Thermochim. Acta.* 602 (2015) 63–73. <https://doi.org/10.1016/j.tca.2014.12.023>.
- [32] Neerad Phansalkar, Sumit More, Ashish Sabale, Madhuri Joshi, Adaptive local thresholding for detection of nuclei in diversity stained cytology images, in: 2011 Int. Conf. Commun. Signal Process., 2011: pp. 218–220. <https://doi.org/10.1109/ICCSP.2011.5739305>.
- [33] C. Flament, J. Ribis, J. Garnier, Y. Serruys, F. Leprêtre, A. Gentils, C. Baumier, M. Descoins, D. Mangelinck, A. Lopez, K. Colas, K. Buchanan, P. Donnadieu, A. Deschamps, Stability of  $\beta''$  nano-phases in Al-Mg-Si(-Cu) alloy under high dose ion irradiation, *Acta Mater.* 128 (2017) 64–76. <https://doi.org/10.1016/j.actamat.2017.01.044>.
- [34] K. Farrell, R.T. King, Tensile Properties of Neutron-Irradiated 6061 Aluminum Alloy in Annealed and Precipitation-Hardened Conditions, *Eff. Radiat. Struct. Mater.* (1979). <https://doi.org/10.1520/STP38180S>.
- [35] K. Farrell, Assessment of aluminum structural materials for service within the ANS reflector vessel, Oak Ridge National Lab., 1995.
- [36] G. Ho, M.T. Ong, K.J. Caspersen, E.A. Carter, Energetics and kinetics of vacancy diffusion and aggregation in shocked aluminium via orbital-free density functional theory, *Phys. Chem. Chem. Phys.* 9 (2007) 4951. <https://doi.org/10.1039/b705455f>.
- [37] T.E. Volin, R.W. Balluffi, Annealing kinetics of voids and the Self-diffusion coefficient in aluminum, *Phys. Status Solidi B.* 25 (1968) 163–173. <https://doi.org/10.1002/pssb.19680250116>.
- [38] Camille Flament, Etude des évolutions microstructurales sous irradiation de l'alliage 6061-T6, Université Grenoble-Alpes, 2015.
- [39] A. Jostsons, R.T. King, Transmutation produced Mg<sub>2</sub>Si precipitation in an irradiated Al-2.5% Mg alloy, *Scr. Metall.* 6 (1972) 447–452.
- [40] D.J. Alexander, The effect of irradiation on the mechanical properties of 6061-T651 Aluminum, in: Philadelphia, 1993.
- [41] K. Farrell, R.T. King et A. Jostsons, Examination of the irradiated 6061 aluminium HFIR target holder, Oak Ridge National Lab., 1973.
- [42] A. Jostsons, Annealing of voids in aluminum, in: *Radiat. Induc. Voids Met. Congr. Proceeding*, 1971.
- [43] K. Farrell, A. Wolfenden, R.T. King, The effects of irradiation temperature and preinjected gases on voids in aluminium, *Irradiat. Eff.* 8 (1971) 107–114.

- [44] R.T. King, E.L. Long, J.O. Stiegler, K. Farrell, High-neutron fluence damage in an aluminum alloy, *J. Nucl. Mater.* 35 (1970) 231–243.
- [45] A. Risbet, Influence des precipites sur la formation des cavites dans un alliage AL 4% CU irradie aux neutrons rapides, *J. Nucl. Mater.* 44 (1972) 113–115. [https://doi.org/10.1016/0022-3115\(72\)90139-0](https://doi.org/10.1016/0022-3115(72)90139-0).
- [46] A. Risbet, Etude de la formation des cavites dans l'aluminium pur et faiblement allie irradie aux neutrons rapides, CEA-Saclay, 1975.
- [47] A. Risbet, V. Levy, Influence de l'ecrouissage sur la formation des cavites d'irradiation dans l'aluminium, *J. Nucl. Mater.* 46 (1973) 341–352. [https://doi.org/10.1016/0022-3115\(73\)90050-0](https://doi.org/10.1016/0022-3115(73)90050-0).
- [48] J. Weeks, C. Czajkowski, P. Tichler, Effects of High Thermal and High Fast Fluences on the Mechanical Properties of Type 6061 Aluminum on the HFBR, *Eff. Radiat. Mater.* 14th Int. Symp. Vol. II. (1990). <https://doi.org/10.1520/STP49465S>.
- [49] B. Jahnke, Porenbildung in einer Al-Mg-Si-Legierung mit unterschiedlichen Ausscheidungszustanden und in Reinstaluminium nach Bestrahlung mit 100 keV Al-Ionen, 1978. <https://publikationen.bibliothek.kit.edu/200011944> (accessed August 12, 2019).
- [50] C. Flament, J. Ribis, J. Garnier, T. Vandenberghe, J. Henry, A. Deschamps, Electron irradiation-enhanced core/shell organization of Al(Cr, Fe, Mn)Si dispersoids in Al–Mg–Si alloys, *Philos. Mag.* 95 (2015) 906–917. <https://doi.org/10.1080/14786435.2015.1009959>.